THE EFFECT OF STRAIN IN MNSI THIN FILMS AND THE STABILITY OF IN-PLANE SKYRMIONS

by

Simon A. Meynell

Submitted in partial fulfillment of the requirements
for the degree of Master of Science

at

Dalhousie University
Halifax, Nova Scotia
August 2017

This thesis is dedicated to my mother who taught me about hard work, dedication and generosity and also to my brother who has taught me about perserverance in the face of an overwhelming ordeal.

Table of Contents

List of Figures

Abstract

Magnetic skyrmions represent a topologically stable field configuration that can arise in magnetic materials that lack centres of inversion symmetry. These solitons have potential applications in digital memory storage because of their ability to be manipulated by currents and because of the fact that their topological stability can imply energetic stability or metastability.

MnSi is a system that has no centre of inversion symmetry and so it is possible to host skyrmions. In MnSi(111)/Si(111) thin films, an epitaxial mismatch induces an in-plane tensile stress which results in a hard-axis magnetocrystalline anisotropy. For in-plane fields, there is controversy surrounding the phase diagram. Yokouchi et al.[76] have used planar Hall effect measurements to claim that a skyrmionic phase does not exist at temperatures of 25 K and fields of $\mu_0 H = 500$ mT, which contradicts previous SQUID magnetometry measurements [74]. The first aim of this thesis is to resolve the controversy surrounding the existence or absence of skyrmions using a less indirect technique.

Polarized neutron reflectometry (PNR) is sensitive to magnetic spatial variation along the depth of the film and so can be used to resolve the presence or absence of skyrmions. A new type of skyrmion lattice in MnSi, one with its axis of symmetry pointing within the plane of the film was uncovered using PNR in conjunction with computational micromagnetic modelling. It was found that the spacing in the lattice was 22 nm, in good agreement with small angle neutron scattering. At lower fields of $\mu_0 H = 300$ mT, the system transitions into a metastable state. This state consists of elliptically extended skyrmions. At higher fields of $\mu_0 H = 700$ mT it was shown that the system exists in a twisted ferromagnetic state.

The viability of SiC(0001) substrates to reverse the sign of the anisotropy was also investigated. The mismatch between MnSi(111) and SiC(0001) is such that the anisotropy might be reversed and result in an easy-axis anisotropy. Reversing the sign of this could result in the stability of out-of-plane skyrmions. The magnetic state of the films was probed using Hall effect measurements and the morphological state was probed using atomic force microscopy. It was found that dewetting instabilities during the growth of MnSi(111)/SiC(0001) result in an in-plane tensile strain and a hard-axis uniaxial anisotropy. Though the dewetting produced an unexpected magnetocrystalline anisotropy, it also produced unusual morphological geometries that could be explored in the future.

List of Abbreviations and Units Used

PPMS	Physical Properties Measurement System
SQUID	Superconducting Quantum Interference Device
MBE	Molecular Beam Epitaxy
DMI	Dzyaloshinskii-Moriya Interaction
RHEED	Reflection High-Energy Electron Diffraction
XRD	X-Ray Diffraction
XRR	X-Ray Reflectivity
PPMS	Physical Properties Measurement System
THE	Topological Hall Effect
IP	In-Plane
OOP	Out-Of-Plane
UHV	Ultra-High Vacuum
PHE	Planar Hall Effect
TEM	Transmission Electron Microscopy
H_D	Bulk Critical Field Between the Cone and Saturated Phase
L_D	The Zero-Excitation Bulk Helical Wavelength
L_{Dy}	The Distance Between Skyrmions in a Lattice
$\vec{H}$	The Applied Magnetic Field
$\vec{B}$	The Total Magnetic Field
R	Reflectivity

n_S	Skyrmion Number Density
N_S	Skyrmion Number
MR	Magnetoresistance
GMR	Giant Magnetoresistance
RM	Racetrack Memory
ω	The Bak-Jensen Free Energy Density
A	The Exchange Energy
D	The Dzyaloshinskii-Moriya Energy
K	The Magnetocrystalline Energy Constant
SANS	Small Angle Neutron Scattering
ML	Monolayer
QL	Quadrilayer
τ_{ML}	Monolayer Arrival Time
m_n	Mass of a Neutron
b	Nuclear Scattering Length
SPE	Solid Phase Epitaxy
STT	Spin Transfer Torque
$\vec{M}$	Magnetization
$\hat{m}$	Magnetic Moment Unit Vector

Acknowledgements

It is clear to me that there is no single greater contributor to my education than my supervisor and friend, Prof. Theodore L. Monchesky. His unwavering support and patience throughout my undergraduate and graduate degrees was truly invaluable. His door seems forever open and he is always willing to discuss a concept you might be struggling with despite the time of night; he has provided an endless source of knowledge and insight into the world of physics and I think this is a rare gift to receive. I count myself truly lucky for having the opportunity to work with him over the past four years and I am eternally indebted to him for his wonderful guidance throughout my undergraduate degree but especially for his help over the past two years with this project.

Though a graduate thesis is usually indebted to those group members who came before, I find myself particularly grateful for the work of Eric Karhu, Murray Wilson and Samer Kahwaji. Without their hard work collecting the neutron data presented in this thesis and perfecting the operation of the MBE it is unquestionably the case that this thesis would not have been possible. Samer Kahwaji, I would like to especially thank because of his willingness to lend a hand with the MBE when Prof. Monchesky was away.

I would also like to thank my student cohort for providing an amazing atmosphere for learning and (occasionally) relaxing. In particular, my lab mates David Kalliecharan and Allison Spitzig have provided irreplaceable help in the smooth operation of the lab. I would also like to thank Kevin Lacaille, Kaja Rotermund, Tim Miller, Andrew Quigley and Marc Cormier for their many insightful and useful conversations throughout my time at Dalhousie. Two honours students who have been particularly helpful in my graduate work are Will Stone and Allister Mason, both of whom did tremendous and illuminating science.

Additionally, I would like to thank Andy George. It sometimes seems every work

produced throughout the department includes Andy George in the acknowledgements and I think that really says a lot. Andy George displays incredible technical versatility and skill in all of the projects he is involved in. I'd also like to thank Kevin Borgel for his help in securing a steady supply of LN_2. Without his ability to navigate the world of cryogenics, it would be impossible to ensure a steady operation of the lab.

There are a number of professors in addition to Prof. Monchesky that I'd like to thank. I'd like to thank Prof. Maassen for taking time out of his busy schedule and agreeing to be a reader. Prof. Robertson at Acadia has provided excellent advice and generously provided the TEM measurements presented within this thesis. Prof. Kreplak has provided the tools and insight possible to do the AFM measurements presented in this work. His patience throughout these experiments was greatly appreciated and I would like to thank him for agreeing to be a reader. In addition to this, I'd like to thank Prof. Rutenberg for his advice and inspiring my fascination with computational and statistical physics.

I would like to thank Tanya Timmins and Stephen Payne for all of the work that they do to ensure the smooth operation of this department. Stephen Payne's facilitation of outreach is of particular value and I would like to thank him for providing the opportunity to be involved with this branch of the department.

It has been my great pleasure to have been a student in this department over the past few years and I believe I am fortunate to have been a part of what I consider to be not only an incredibly intellectually enriching experience but also a very happy one. Finally, I feel as though I should offer thanks to the entire Physics Department at Dalhousie for providing this exceptional experience.

Chapter 1

Introduction

Spin transport electronics, or spintronics as it is commonly known, began in the 1980's. One of the first major developments in this field was the discovery of giant magnetoresistance (GMR) by Baibuch et al. [1] and Binasch et al.[8] of the Fert and Grünberg groups respectively. The 2007 Nobel Prize in Physics would be awarded nearly 20 years later to Fert and Grünberg for this discovery. This still growing field has led to many commercial applications such as magnetic memory devices and hard-disk read-heads.

GMR is an effect whereby the resistance between ferromagnetic layered films will change depending on the orientation of the alignment of the magnetization between the layers. Though this effect was first discovered in Fe and Cr films and was found to be a 79% effect, many other materials, such as Fe/MgO/Fe and CoFeB/MgO/CoFeB, were discovered soon after [78][29]. These were found to have GMR effects of up to 604%. One way to exploit this effect is with a spin valve[15]. In a spin valve, one of the ferromagnetic layers is pinned by an adjacent antiferromagnetic layer and the other ferromagnetic layer is free to switch on the application of a magnetic field. By having the layers parallel or antiparallel, information can be stored and read electrically [68].

Spin-transfer torque (STT) is another important effect in the field of spintronics [57]. This effect was originally proposed in 1996 independently by both Slonczewski [60] and Berger [6]. STT refers to the process whereby a spin-polarized current is able to transfer angular momentum and influence the orientations of magnetizations. The first theoretical and experimental consideration involved domain wall movement [5][19]. At first, this work was largely ignored because of the high current density required to move the domain walls and the relatively large prerequisite sample sizes at the time[57]. Later on, around the turn of the millennium, with the advent of more

advanced fabrication techniques more commercially viable implementations of STT were discovered [21][67]. A modern implementation of STT in the area of magnetic memory involves an array of layered devices, each with one "fixed" ferromagnetic layer and a thinner "free" ferromagnetic layer. Usually a current is unpolarized, upon passing the current through a first ferromagnetic layer, the current will become polarized in the direction of the first ferromagnetic layer. This polarized current will then interact with a thinner free layer and transfer some angular momentum to that layer by way of STT [37]. Another implementation of STT in magnetic memory is racetrack memory (RM), a type of non-volatile magnetic memory that was developed at IBM's Almaden Research Center by the Parkin group in 2008 [25]. This type of memory involves magnetic domains arranged on a wire. In this shift-register-like approach to memory, domains are shifted up and down the track using currents and read out electrically. One of the potential downsides with this technology was that domain walls would easily become stuck on defects while in transit [39].

Though domain walls are potentially useful spintronic solitons, a newer magnetic pseudoparticle, called a magnetic skyrmion, has emerged in recent years as a promising new object. Originally this field configuration was proposed by Tony Skyrme in 1962 as a model for nucleons in the pion field [59]. The non-linearities produced by chiral and other interactions in condensed matter systems have been found to produce analogous solitons inside materials. Topologically stable field configurations for Skyrmion-like objects have been proposed in chiral liquid crystals [11][40] and Bose-Einstein condensates [62].

Skyrmions in magnetic crystals were first proposed by Bogdanov et al. in 1989 [12] and later predicted to exist in cubic helimagnets by Rößler *et al.* in 2006 [58]. In 2009 magnetic skyrmions were first experimentally verified in bulk MnSi using neutron scattering techniques and then further investigated using Hall effect measurements [53][45][54]. Skyrmion crystals were subsequently observed in real space using Lorentz transmission electron microscopy (TEM) by Yu *et al.* [77] in 2010. These skyrmions have been proposed as alternatives to domain walls in RM because of their ability to

navigate around defects and their low power requirements [18]. At present, the new field of skyrmionics (the spintronics of skyrmions) is rapidly increasing in size and notability. Recently, spin logic gates have been designed in order to perform logical operations using skyrmions [79]. Both AND and OR gates have been designed based on the manipulation of skyrmions, further broadening the scope of potential skyrmion applications. In 2015, Tokunaga et al. [66] discovered a new class of materials that are able to host magnetic skyrmions beyond room temperature, demonstrating that in principle, skyrmions are capable of existing in room temperature applications.

1.1   The Bak-Jensen Free Energy

Magnetic skyrmions (hereafter referred to as simply, skyrmions) are a topologically protected magnetic spin configuration in which the central spin points antiparallel to the applied field. Typically a skyrmion will have close to radial symmetry and a one-dimensional slice through any direction will have a domain-wall character. There are a variety of types of skyrmions such as Néel-type skyrmions whose radial slices have the appearance of Néel walls and Bloch-types that are somewhat vortex in character. A radial slice through one of these shows winding like a Bloch domain wall. There are even anti-skyrmions that do not have radial symmetry and whose character has a directional dependence. Whether or not a type of skyrmion is stable or not is determined by the precise symmetry class of the crystal. The type I will be referring to in this thesis are Bloch-type skyrmions, as shown in fig. 1.1.

The micromagnetic model used in order to understand skyrmionic stability is the Bak-Jensen free energy density, [2],

$$\omega = A(\nabla \hat{m})^2 + D\hat{m} \cdot \nabla \times \hat{m} - K(\hat{m} \cdot \hat{n})^2 - \mu_0(\vec{H}_{ext} + \frac{1}{2}\vec{H}_d) \cdot \vec{M}. \qquad (1.1)$$

The first term in the model is the exchange energy, $A(\nabla \hat{m})^2$. Here $(\nabla \hat{m})^2$ is the usual notation meaning,

$$(\nabla \hat{m})^2 = (\nabla m_x)^2 + (\nabla m_y)^2 + (\nabla m_z)^2. \qquad (1.2)$$
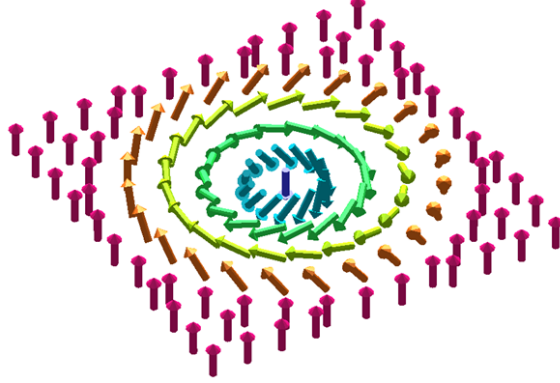
Figure 1.1: The spin configuration of a magnetic skyrmion. The arrows represent the direction of the local magnetic moment. Skyrmions represent a topologically stable field configuration.

This is a term that is quantum mechanical in origin and results from generalizing the spin-exchange Hamiltonian,

$$\mathcal{H}_{spin} = -2J\vec{S}_i \cdot \vec{S}_j, \tag{1.3}$$

to a continuum model. The constant, $A = 2JS^2z/a$, where a is the nearest neighbour distance and z is the number of sites per unit cell [10]. This constant has units of energy per unit length and typical values are $\sim 10^{-13}$ N. The exchange energy is lowest when there is no variation in the magnetization with respect to space. In other words, the exchange interaction will have lowest energy when all the spins are parallel to each other.

The next term in the free energy is the Dzyaloshinskii-Moriya interaction [16][52]. This term is a continuum generalization of the DMI Hamiltonian,

$$\mathcal{H}_{DMI} = \vec{D}_{ij} \cdot (\vec{S}_i \times \vec{S}_j). \tag{1.4}$$

This was originally proposed on phenomenological grounds based on Landau theory by Dzyaloshinskii. It was later identified as being the result of spin-orbit coupling by Moriya. This term is a chiral interaction which appears in systems that have broken inversion symmetry. The vector $\vec{D}_{ij}$ is in general non-zero but must vanish if the

4

material has any centres of centrosymmetry. This term will be either a maximum or a minimum when the spins are oriented 90° with respect to each other. In the continuum model this interaction takes the form, $D\hat{m}\cdot\nabla\times\hat{m}$. Where D is a constant with units of energy per unit area and the sign of which will determine the handedness of the preferred winding. Typical values of D are $\sim 10^{-6}$ N/m. Since the DMI is lowest when the spins are changing rapidly in space and exchange is lowest when the spins vary little, we can combine the constants to get a length scale for magnetic variation. Upon minimizing the free energy, one finds the wavelength of winding is $L_D = 4\pi A/D$. Values of L_D vary between materials but are typically in the 10's to 100's of nm range.

The third term in this model, $-K(\hat{m}\cdot\hat{n})^2$ represents the uniaxial magnetocrystalline anisotropy where $\hat{n}$ is a unit vector along the film normal. In many materials, magnetizing along certain crystallographic directions is harder than others. The most common anisotropic effect is uniaxial, where there is only one easy or hard direction. K has units of energy per unit volume and is defined to be positive for materials that are easy-axis and negative for materials that are hard-axis. Typical values of K are $\sim 10^4$ J/m^3. The origin of this term is spin-orbit interaction. Since for uniaxial anisotropy we can have no rotational dependence, our free energy can only depend on the azimuthal angle, θ. This means that the natural expansion is a series of sines. The free energy will then be, $\omega_K = K_0 + K_1\sin^2\theta + K_2\sin^4\theta + K_3\sin^6\theta + ...$ Taking only terms up to $\sin^2\theta$ and recognizing that any constant terms can be ignored, we arrive at the familiar expression $-K(\hat{m}\cdot\hat{n})^2$ [10]. The effect of temperature on anisotropy is such that it becomes less important at higher temperatures. This is because a spin will sample an ensemble of angles at any given time due to the finite temperature. This has the effect of lowering the extreme values of the anisotropy along the easy and hard directions. Since only energy differences are relevant, this has the effect of making anisotropy a less important term as the temperature is increased. Uniaxial anisotropy is different than cubic anisotropy in that there is only one relevant direction. Because MnSi is cubic it will have cubic anisotropy, although for thin films this

is small compared to the uniaxial anisotropy and is neglected.

The final term in this free energy is the sum of Zeeman energy and the demagnetizing field energy, $-\mu_0(\vec{H}_{ext} + \frac{1}{2}\vec{H}_d) \cdot \vec{M}$. The Zeeman energy, $-\mu_0\vec{H}_{ext} \cdot \vec{\mu}$, was discovered in 1896. The atom's dipole moment is $\vec{\mu}$ and $\vec{H}_{ext}$ is an external magnetic field. In the continuum model, this interaction has the lowest energy when the magnetization is aligned with the external field. The demagnetizing field is a result of the fact that the magnetization will induce a magnetic field. Calculating $\vec{H}_d$ can be done by considering Ampere's law, $\nabla \times \vec{H} = 0$ and the no magnetic monopoles law, $\nabla \cdot \vec{B} = 0$. We use the relations $\vec{H} = \vec{H}_{ext} + \vec{H}_d$ and $\vec{B} = \mu_0(\vec{H} + \vec{M})$. Ampere's law motivates the introduction of the magnetic potential, $\vec{H} = -\nabla U_m$. Solutions can be found by solving $\nabla^2 U_m = \nabla \cdot \vec{M} = \rho_m$. Using the fictitious magnetic charge density, ρ_m, demagnetizing field problems can be mapped on to electrostatic problems. The energy of the demagnetizing field is given by $-\mu_0\vec{H}_d \cdot \vec{M}/2$, where the factor of $1/2$ is due to the fact that the field is generated by the magnetization itself and is to avoid double-counting. Because dipole fields are long range interactions this term is usually difficult to calculate. Fortunately, it is often small compared to DMI and can be neglected [38].

1.2 Helimagnets and Skyrmions

The first and simplest solution to the Bak-Jensen free energy functional is for a helimagnet in 0-field and with no anisotropy. In this case the functional form which minimizes the free energy is a helical winding of the magnetization. The function that minimizes the free energy can be found using calculus of variations but for expediency's sake, we can begin with a helical magnet *ansatz*,

$$\vec{M} = M_S\hat{m} = M_S(\cos(2\pi z/L_D), \sin(2\pi z/L_D), 0). \tag{1.5}$$

The total free energy for a magnetic system that only varies in the z-direction and with only in-plane components, will be given by,

$$F = \int_{vol} d^3r A[(\frac{dm_x}{dz})^2 + (\frac{dm_y}{dz})^2] + D[m_y\frac{dm_x}{dz} - m_x\frac{dm_y}{dz}]. \tag{1.6}$$

Substituting the helical magnet in we get,

$$F = \int_{vol} d^3r A\frac{4\pi^2}{L_D^2} - D\frac{2\pi}{L_D}, \tag{1.7}$$

and minimizing with respect to L_D gives us the solution for the helical wavelength, $L_D = 4\pi A/D$. The introduction of a non-zero field and anisotropy complicates the analysis.

The application of a field along the propagation direction will begin to cant the spins along the field direction. This is called the cone-phase because the helical state cants upwards in cone-like fashion. The cone angle, θ, is defined to be the angle between the x-y plane and the spins. This angle will increase with the application of an out-of-plane field until it saturates into a ferromagnetic state. The angle can be calculated using an updated ansatz,

$$\vec{M} = M_S\hat{m} = M_S(\cos(2\pi z/L_D)\cos\theta, \sin(2\pi z/L_D)\cos\theta, \sin\theta), \tag{1.8}$$

where θ is the cone-angle and does not vary spatially. Our new free energy will be given by,

$$F = \int_{vol} d^3r A[(\frac{dm_x}{dz})^2 + (\frac{dm_y}{dz})^2] + D[m_y\frac{dm_x}{dz} - m_x\frac{dm_y}{dz}] - \mu_0 H M_Z. \tag{1.9}$$

Minimizing with respect to the cone angle will give us,

$$\theta = \arcsin(\frac{2\mu_0 AHM_S}{D^2}). \tag{1.10}$$

This conical state will transition into a ferromagnet when $\theta = 90°$. The field at which

7

this transition happens will be given by, $\mu_0 H_D = D^2/2AM_S$.

Skyrmion stability is a more complicated question but can be answered by examining the anatomy of a skyrmion and considering the various interactions involved. A skyrmion consists of a core that costs a substantial amount of energy due to the Zeeman interaction and an energetically favourable ring region where the magnetization winds around the core. It is the DMI that stabilizes the ring region. As the external field increases in magnitude, the cost of the core increases and what is usually observed is that the skyrmion contracts in size. A skyrmion and the energetic components are shown in fig. 1.2. Figure 1.2 a) shows the spin distribution of an isolated skyrmion with the external field pointing in the x-direction. A line profile through the centre of the skyrmion would display a helical like distribution of spins. The energies are given in terms of differences between a skyrmion phase and the ferromagnetic background. Figures 1.2 b) shows the Zeeman energy difference and c) shows the difference between the sums of the exchange and DMI energy for a skyrmion and twisted ferromagnet phase. The total energy difference between these phases is given in fig. 1.2 d) and demonstrates the energetically unfavourable core with the favourable ring. Total energy for this system of size 25.6 nm× 51.2 nm× 0.2 nm is -1.2 meV.

Skyrmions are of particular interest because of their non-trivial topology. A field of a certain topology can never be continuously deformed into a field of a different topology. Since a skyrmion is topologically distinct from other phases in a helimagnet, this means that a discontinuous transition is needed during a phase change. Analogous to a winding number, a skyrmion has what is called a topological charge. The topological charge of an object is quantized and corresponds to the number of times a vector field's vectors can completely cover a unit sphere. For a skyrmionic phase, the topological charge (and skyrmion number) will be given by,

$$N_s = \int_{area} dxdy \frac{1}{4\pi} \hat{m} \cdot \left(\frac{\partial \hat{m}}{\partial x} \times \frac{\partial \hat{m}}{\partial y} \right), \tag{1.11}$$

and corresponds to the number of skyrmions within a certain area [9].

8
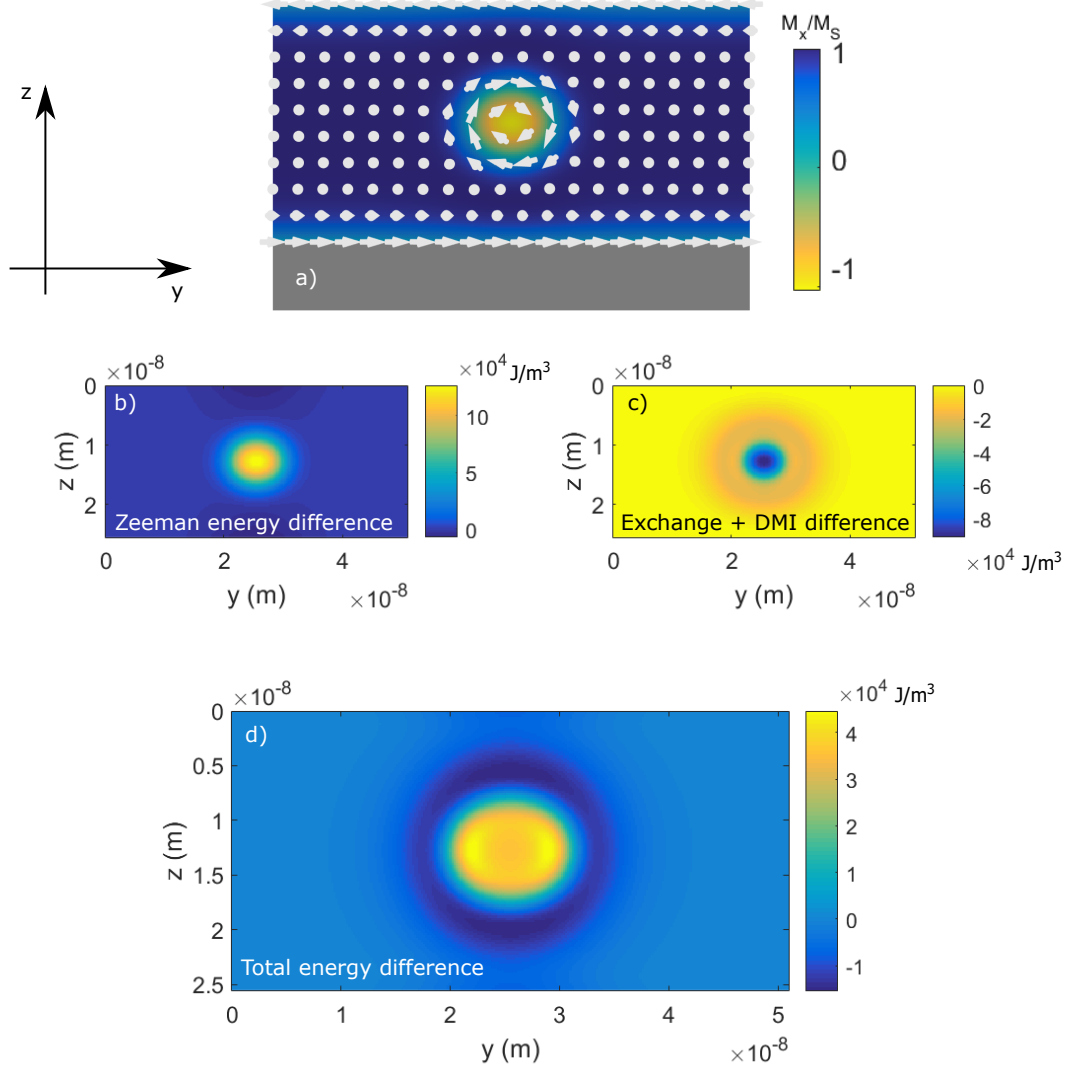
Figure 1.2: The energy density difference between a skyrmion and the twisted ferromagnetic background for a system of size 25.6 nm× 51.2 nm× 0.2 nm. The spin distribution for a skyrmion is shown in a). Skyrmions are composed of an energetically favourable ring and an energetically costly core. The Zeeman energy difference is shown in b) and is highest for the skyrmion core because it points in the opposite direction of the applied field. The difference between the sum of the exchange and DMI energy for a skyrmion and a twisted ferromagnet is shown in c) and is lowest in the centre of the skyrmion. The total energy difference is shown in d) and shows the energetically unfavourable core with the favourable ring. The integral of this gives an energy of -1.2meV.

9

In practice, topological stability does not necessarily imply energetic stability between phases with differing topological charges. The discrete nature of matter means that a continuum model of magnetization is never wholly accurate and so there can never be an infinite energy barrier due to differences in topological charge. However, topological stability can imply the existence of large but finite energy barriers between competing phases. This means that skyrmions act like metastable particles and can be moved by STT mechanisms through electrical currents. In 2015, Hanneken et al. [24] demonstrated a new technique that exploits the fact that a skyrmion locally alters the electronic structure through mixing of the spin channels. This allows the presence or absence of a skyrmion to be read through electrical means.

1.3 Bulk MnSi

MnSi is a weak itinerant ferromagnet with a moment of $\mu_{bulk} = 0.39\mu_B/$Mn below its Curie temperature of $T_C = 29.5$ K. It has a cubic B20 crystal structure with the space group P2$_1$3 (number 198). This structure has a lattice parameter of $a_{MnSi} = 0.4561$ nm. The structure has basis vectors at (u, u, u),$(1/2 + u, 1/2 - u, -u)$,$(-u, 1/2 + u, 1/2 - u)$, and $(1/2 - u, -u, 1/2 + u)$ with $u_{Mn} = 0.135$ and $u_{Si} = 0.845$. There are no centres of inversion within this crystal structure [35][30]. The crystal structure is shown in fig. 1.3. A view along the [111]-direction is shown in a), the [110]-direction in b) and the [100]-direction in c). A unit cell is shown along an arbitrary direction in d).

Because of the lack of inversion symmetry, the DMI is non-zero in MnSi. This leads to a helimagnetic state below the Curie temperature. The magnetic structure will break up into four helical domains oriented along the four <111>-cube diagonals[23]. An applied field will align the domains at $\mu_0 H_{C1} \approx 0.1$ T when the system transitions into the cone phase. As the field increases, the system transitions from a conical magnet into a saturated ferromagnetic state. This critical field is called $\mu_0 H_{C2} \approx 0.6$ T. A skyrmion phase has been identified in a small pocket of the phase diagram, sometimes referred to as the "A-phase". The controversial region was conclusively determined
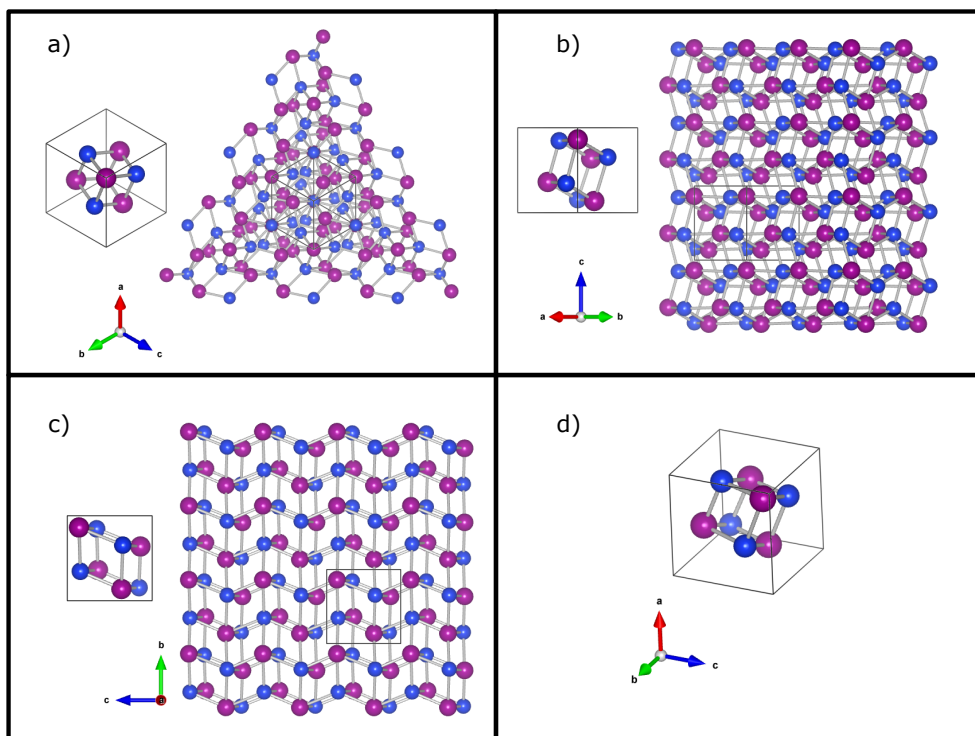
Figure 1.3: Crystal structure of MnSi has viewed along the [111]-direction a), the [110]-direction b) and the [100]-direction c). A unit cell is shown in d) along an arbitrary direction.
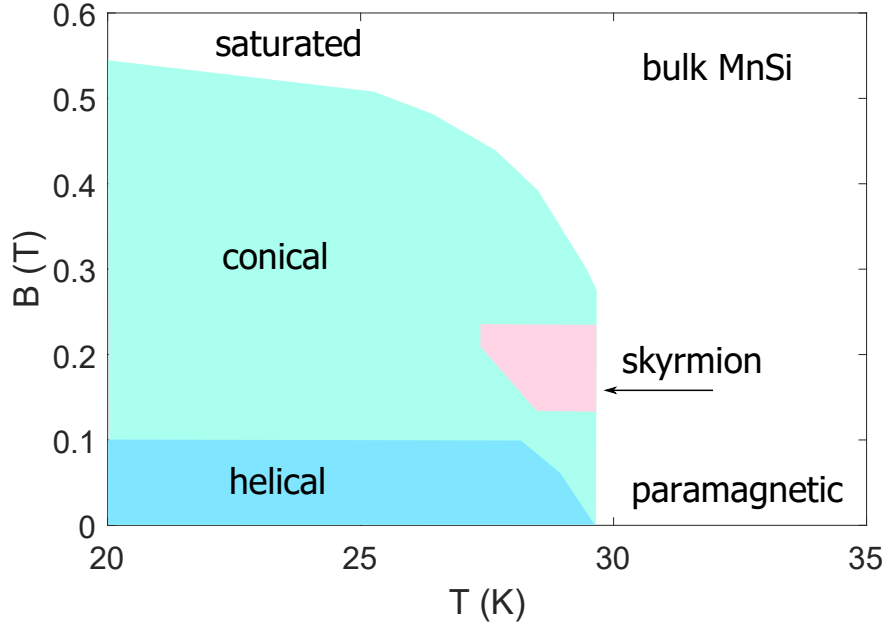
Figure 1.4: Magnetic phase diagram for bulk MnSi, adapted from Ref. [55]. Above the Curie temperature, the system exists in a paramagnetic state. Below this temperature the system is more complicated. For low fields the system exists in a mixed-phase helical state but as the field increases it transitions to a conical state. Eventually the system saturates at $\mu_0 H_{C2} = 0.6$ T. A skyrmion phase has been identified in a small pocket close to T_C.

to be due to a skyrmionic phase after Mühlbauer et al. [45] probed the region with small angle neutron scattering (SANS) and Hall effect measurements [53]. Figure 1.4 shows the phase diagram for bulk MnSi at ambient pressure adapted from ref. [55]. This pocket of stability has been shown to increase in size in the presence of pressure [14].

1.4   Thin Film MnSi

Work done by Butenko et al. [13] in 2010 suggested that inducing uniaxial anisotropy in noncentrosymmetric cubic helimagnets, such as MnSi, could result in a stabilization of skyrmionic phases. Uniaxial distortions can be induced by epitaxial mismatch and so the prospect of epitaxially induced mismatch in thin films emerged as a possibility for MnSi. Because the surface lattices of MnSi(111) and Si(111) are well-matched
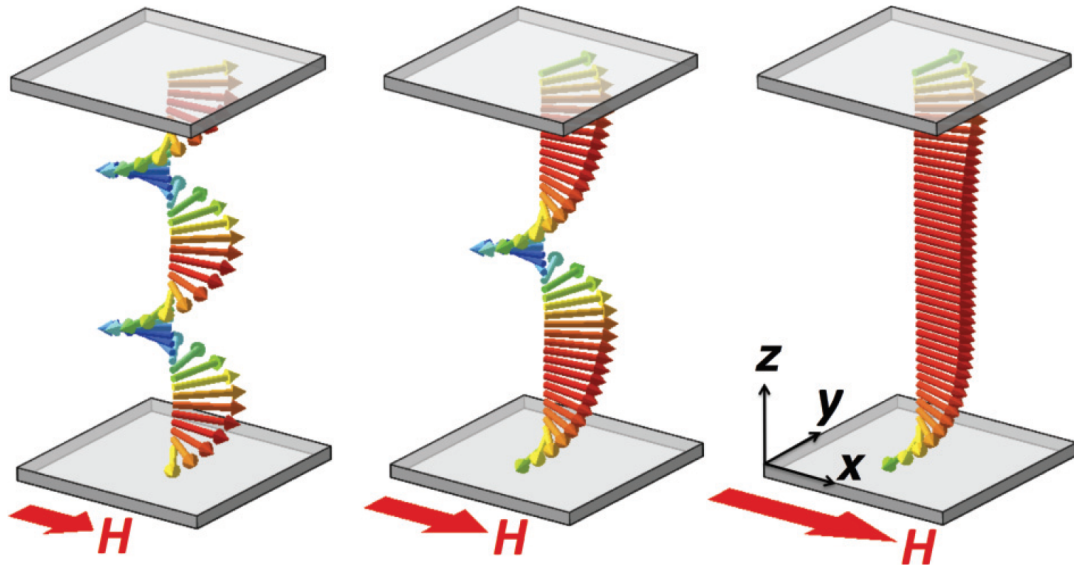
Figure 1.5: For in-plane fields at low temperatures, one dimensional solutions to the Bak-Jensen functional for a thin film are discretized. As the field is increased in-plane, the system will transition discontinuously between a discrete number of twists [73].

(as discussed in section 2.1.2), Si(111) emerged as a viable candidate for thin film growth. The lattice mismatch is 3% and is tensile in nature. In 2010 Karhu et al. found this type of growth led to an enhanced Curie temperature of $T_C \approx 40$ K which was closely correlated to a volumetric expansion of the unit cell [32]. It was found that this tensile strain resulted in an out-of-plane hard-axis magnetocrystalline anisotropy. The magnetic state with 0 field and at $T = 5$ K was found to be a helical magnet with the propagation vector pointing along the film normal in the [111]-direction. The wavelength of the helix was found to be 13.9 ± 0.1 nm.

For out-of-plane fields, the system was found to be in a conical state. In this case, both the anisotropy and demagnetizing field add corrections to the saturation field [33]. For in-plane fields the situation is more complicated. The film boundaries prevent the reorientation that occurs in bulk crystals and for one-dimensional solutions, the system undergoes an unwinding that occurs in discrete steps [73]. As the field is increased at a temperature of 5 K, it has been shown that the helix will unwind discontinuously. These one-dimensional solutions are shown in fig. 1.5.

It was also found that SQUID magnetometry suggested a skyrmionic phase for in-plane fields. These skyrmions differ from the usual skyrmions because they have their radial axis of symmetry pointing parallel to the field direction rather than perpendicular to the plane [74]. The phase diagram for in-plane fields in MnSi(111)/Si(111) as determined by SQUID is shown in fig. 1.6. Here the filled circles correspond to peaks in dM/dH measured for decreasing fields and the unfilled circles correspond to increasing fields. The blue squares correspond to minima in d^2M/dH^2.

Though the magnetometric measurements ruled out any skyrmionic phase for out-of-plane fields, Hall measurements carried out by Li et al.[42] suggested an electrical effect that was initially interpreted as skyrmionic in origin. Subsequent electrical measurements by Meynell et al. [49] found that the signal in question was due to the cone phase and was not correlated with a transition to a skyrmion phase.

The blue region in fig. 1.6 corresponds to a controversial region of the phase diagram. Yokouchi et al. [76] have conducted planar Hall effect (PHE) measurements and have found a signal that was interpreted as being skyrmionic in origin. Additionally, their measurements in the region marked "Skyrmion" have not found a PHE. Yokouchi et al. have interpreted this as evidence against a skyrmionic phase. These measurements are in direct contradiction to polarized neutron reflectometry (PNR) measurements taken in the 5 K region [73], denoted by the yellow triangles, and SQUID magnetometry measurements [34]. Because the SQUID magnetometry measurements as well as the PHE measurements are both relatively indirect, there is motivation for a more direct probe of the skyrmion phase. The stars correspond to the regions where the polarized neutron reflectometry measurements presented in this thesis were performed. Because of the ability to resolve magnetic variation in PNR, this technique will be able to resolve the controversy surrounding this region.
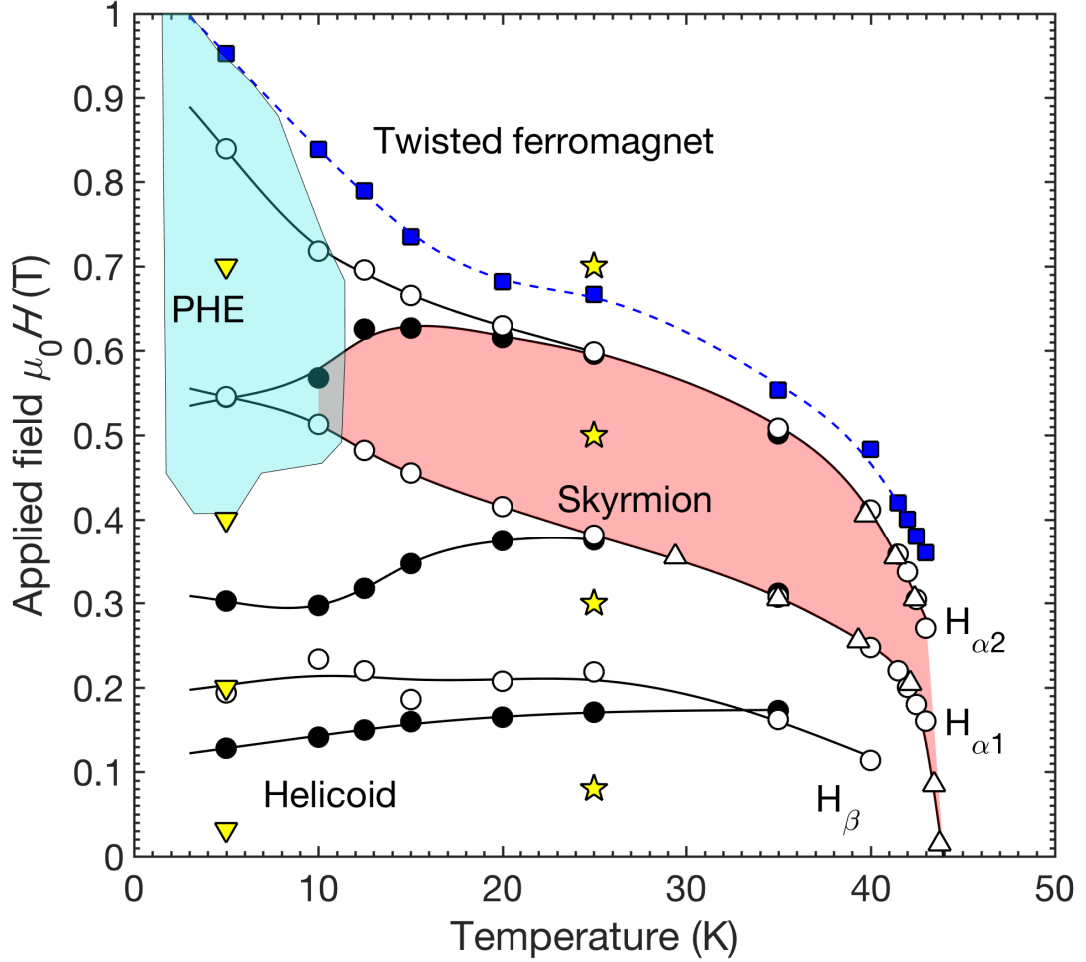
Figure 1.6: The phase diagram for MnSi/Si(111) film for in-plane fields ($\vec{H} \parallel [1\bar{1}0]$) [48]. The filled circles correspond to peaks in dM/dH for decreasing fields. The un-filled circles are peaks for increasing fields. The blue squares are minima in d^2M/dH^2 for increasing magnetic fields. The stars represent the points in the phase diagram that were probed with polarized neutron reflectometry (PNR) measurements. The yellow triangles were probed by PNR in Ref. [73]. The cyan region represents a region that has been interpreted as skyrmionic by Ref. [76] due to PHE measurements.
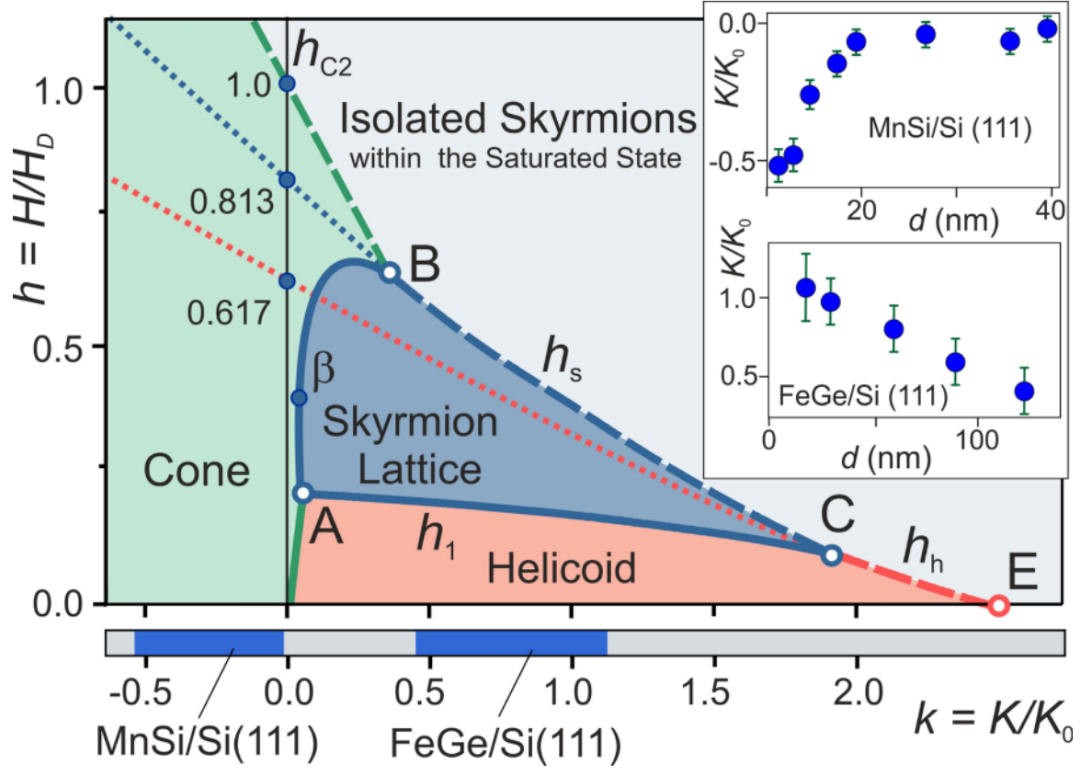
Figure 1.7: Solutions to the Bak-Jensen functional for out-of-plane fields with the field and anisotropy as independent variables taken from ref. [72]. The field has been normalized by H_D and the anisotropy has been normalized by the effective anisotropy $K_0 = D^2/(4A)$. Filled areas represent regions of stability while the lines represent critical lines for metastability. For MnSi/Si(111), the system has easy-plane anisotropy (negative k) and so is expected to remain in the conical phase. For MnSi/SiC(0001), the expectation is that k will be positive and a wider variety of magnetic phases will be available for out-of-plane fields.

1.4.1 SiC

SiC has a hexagonal lattice with the space group $P6_3m$ (number 186) and presents an interesting opportunity for an epitaxial substrate. This is because the lattice mismatch between SiC(0001) and MnSi(111) is compressive rather than tensile. Density functional calculations indicate that a strain sign reversal is needed to change the hard-axis anisotropy found in MnSi/Si to an easy-axis anisotropy [34]. An easy-axis anisotropy will help stabilize skyrmions for out-of-plane fields. A phase diagram with applied field on the vertical axis and anisotropy on the horizontal axis is shown in fig. 1.7.
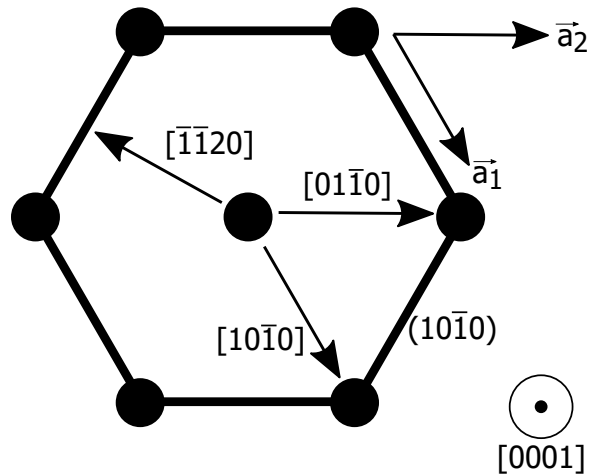
Figure 1.8: Hexagonal crystallographic directions. For hexagonal crystals a fourth miller index, $i = -(h + k)$, is often used. The directions for a hexagonal lattice are shown using the convention $[hkil]$. The reciprocal planes have their normals rotated $30°$ with respect to the corresponding crystallographic direction in contrast to cubic where these directions are parallel. The $(10\bar{1}0)$ plane is labelled in the figure for reference.

In hexagonal systems a special notation is often used for clarity. A fourth Miller index is added that is equal to $i = -(h + k)$ and directions are denoted $[hkil]$. This is so that directions that are symmetric under rotational transformations take on identical miller indices. For example, the direction with $h = 1, k = 0, l = 0$ would be denoted $[10\bar{1}0]$. This direction is, under a rotation, the same as the direction with $h = 1, k = -1, l = 0$ which would be denoted by $[1\bar{1}00]$. With the additional i-index, these two equivalent directions take on similar Miller indices. Because the system is hexagonal, extra care must be taken when dealing with crystallographic directions and the corresponding reciprocal lattice vectors. Unlike in a cubic system where the $[1\bar{1}0]$-direction is normal to the $(1\bar{1}0)$-plane, in a hexagonal system the $[10\bar{1}0]$-direction is offset by $30°$ to the $(10\bar{1}0)$-plane normal. This geometry is shown in fig. 1.8.

17

Chapter 2

Methods

2.1 Sample Preparation

Samples were grown with molecular beam epitaxy (MBE), a thin film fabrication technique that takes place in ultra-high vacuum (UHV), with a base pressure of $\sim 10^{-11}$ torr. The UHV environment of MBE leads to exceptionally pure single crystal films but requires slower deposition rates than other methods.

Typically the deposition material is heated until it sublimes and then will eventually condense on to the substrate. The MBE environment is sufficiently low pressure that the mean free path of the deposited material is typically much larger than the distance to the substrate. In the ideal case, films will grow layer-by-layer. A deposited adatom will move around the surface from site to site until it finds a step edge. This leads to epitaxial growth whereby a single crystal can grow nearly perfectly.

While the early work done in skyrmionics focused on behaviour in bulk crystals, MBE provides an excellent opportunity to probe finite-size effects. Boundaries and other defects are very important for understanding skyrmion confinement [47], skyrmion nucleation[44] and skyrmion stabilization[74].

2.1.1 Molecular Beam Epitaxy

The mechanism by which crystals are grown in MBE is through beams of particles that do not interact with the background vapour and eventually arrive on the substrate. These beams are usually formed by evaporating material from a reservoir that is heated by an electron beam or radiative transfer by a filament. Deposited material arrives at relatively slow rates on clean, single crystal wafers. If the deposited material has a lattice constant close to that of the underlying substrate, it is possible to grow

films atomic layer by atomic layer such that extremely smooth, single crystal films are obtained.

The UHV environment typical of MBE is necessary to reach the high purities required for single crystal growth. These low pressures result in mean free paths typically far greater than the chamber itself, resulting in the beam-like character of the sublimated atoms. A schematic of the MBE system used is shown in fig. 2.1.

The substrate is mounted in a 4" substrate holder that offers support for the wafer around the edges. This is placed in the sample manipulator which allows the experimenter to rotate the sample during growth and allows electrical access for the heating unit which is mounted above the substrate. A thermocouple is attached to the top side of the heater. The manganese is deposited by a home built effusion cell. By changing the current running through the filament and hence the temperature, the deposition rate can be controlled. The manganese deposition rate is monitored through the use of an ion gauge that is calibrated ahead of time. The silicon is deposited using an water-cooled electron beam (e-beam) evaporator. An e-beam evaporator generates a continuous beam of electrons from a filament that strike a puck of material and heat it until sublimation. The deposition rate of silicon is measured through the use of a quartz oscillator. Mechanical shutters are able to block the beam and are used to control the timing of the growth.

The low pressures inside the MBE chamber allow for powerful *in-situ* measurement techniques such as reflection high-energy electron diffraction (RHEED). A beam of glancing incidence electrons are scattered from the sample and the diffracted electrons are imaged with a phosphorescent screen. This allows the experimenter to monitor the quality of the growth during the sample creation process.

The mean free path can be estimated by considering the probability that an atom strikes the background gas whilst travelling through a thin slab with depth dx [71]. The total number of atoms per unit volume is n and the cross sectional area of a single gas atom is σ, the gas will occupy an area, A_{gas} and the total area of the slab
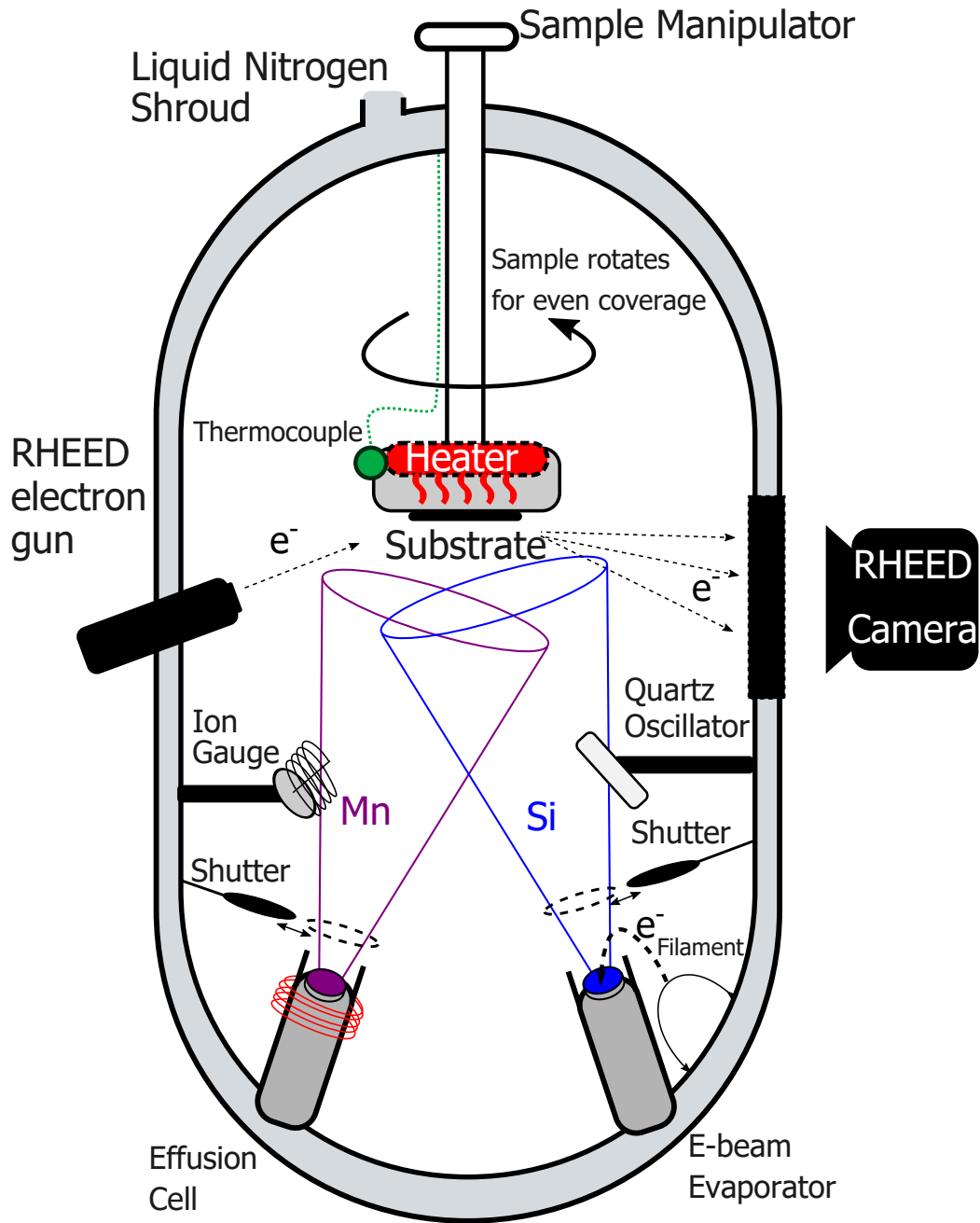
Figure 2.1: Schematic for the molecular beam epitaxy system used to grow the MnSi thin films presented in this thesis. The system is held in ultra-high vacuum in order to ensure a clean growth. The sample is held on the manipulator and the temperature is controlled with a heating element. A shroud encasing the vacuum chamber is filled with liquid nitrogen in order to reduce the background pressure. The growth is monitored using reflection high energy electron diffraction. Mn and Si are deposited using an effusion cell and e-beam evaporator respectively. The Mn and Si deposition rates are monitored using an ion gauge and a quartz oscillator respectively.

will be, A_{total}. The probability of a collision, P_c, will then be given by,

$$P_c = \frac{A_{gas}}{A_{total}} = \sqrt{2}\sigma n dx, \tag{2.1}$$

where the $\sqrt{2}$ is a geometric factor due to thermal motion. The intensity attenuation of a beam of atoms will then be given by,

$$\frac{dI}{dx} = -\sqrt{2}I\sigma n = \frac{-I}{\lambda}, \tag{2.2}$$

where λ is defined as the mean free path. Using the ideal gas law, $P = nk_BT$, we can then arrive at,

$$\lambda = \frac{k_BT}{\sqrt{2}\sigma P}. \tag{2.3}$$

Solving for the pressure under the assumption of room temperature and a molecular cross-sectional area of ~ 0.1 nm^2 with the requirement of $\lambda \geq 1$ m gives us $P \leq \sim 2 \times 10^{-4}$ torr [71]. This is much higher than typical UHV pressures and so we can safely assume that particles travel in almost entirely ballistic trajectories.

The more important and difficult to meet requirement is that of high purity. Gaseous material within the chamber will naturally result in the nucleation of defects by adsorption. In order to understand how this restricts the pressure we need to estimate the time-scale over which adsorbate arrival on the film due to the background pressure. This time is called the monolayer (ML) arrival time and is given by, τ_{ML} [56]. Because a typical MBE growth happens on a time frame on the hour scale, it is important that the (ML) arrival time is not less than an hour. First we must calculate the molecular flux of all particles with velocity, v that are a distance Δx away arriving on a substrate of area, A in a time interval, Δt. We will constrain the velocity such that, $v = \Delta x/\Delta t$. The flux will then be given by,

$$\Phi = \frac{N}{A\Delta t} = nv, \tag{2.4}$$

where n is the number of particles per unit volume. However, the particles will follow

a Maxwell-Boltzmann-distribution and so we must multiply by the probability of a particle having a particular velocity and integrate over this velocity distribution. We get,

$$\Phi = \int_0^\infty nv^3 \sqrt{\frac{2m^3}{\pi k_B T}} \exp(-mv^2/2k_B T) dv = n\sqrt{\frac{k_B T}{2\pi m}}, \tag{2.5}$$

where m is the mass of the particle. Finally, in order to find the ML arrival time we need to take this flux and substitute the ideal gas law and the relation $\Phi = N_{ML}/A_{ML}\tau_{ML}$, where N_{ML}/A_{ML} is the number of atoms in a ML per unit area. We get an expression for the ML arrival time,

$$\tau_{ML} = \frac{\sqrt{2\pi k_B T m}}{P} \frac{N_{ML}}{A_{ML}}, \tag{2.6}$$

and importantly, we can see that τ_{ML} is inversely proportional to the background pressure. CO, a common MBE adsorbate, has a mass of 28 Da and a ML surface density of $N_{ML}/A_{ML} \approx 1 \times 10^{19} m^{-2}$. Restricting $\tau_{ML} \geq 1$ hr, gives us the criteria, $P \leq 7 \times 10^{-10}$ torr. This is the primary reason MBE requires such high vacuum. Since impurity arrival time (and hence, impurity concentration in the sample) is inversely proportional to the background pressure, it is very important to have the lowest background possible.

Achieving UHV pressures is a difficult process and evacuation must occur over multiple steps. First a scroll pump and a turbo pump work to get the pressure into the micro-torr range. After this a cryopump is turned on and is able to reach nano-torr levels. Before a growth can occur, it is necessary to perform a bake-out, where the entire system is heated at temperatures of $\sim 150°\text{C}$ to reduce the pressure into the mid 10^{11} torr range. During a growth, the last technique used to achieve the lowest possible pressures involves filling a jacket surrounding the chamber with liquid nitrogen. This causes any remaining background gasses to condense on the walls of the system for the duration of the growth and with this, the experimenter is able to achieve pressures of the necessary low pressures for the growth.

2.1.2   MnSi/Si

The MnSi/Si sample studied in this thesis was grown by Dr. Eric Karhu on 300 μm thick Si(111) wafers. These wafers were cleaned in an ultrasonic bath of first acetone, followed by methanol and then in an H_2O_2/NaOH base piranha solution.

The wafer was annealed at 600°C overnight to degas the sample. The native Si oxide was then removed by heating up to 800°C for approximately 1 hour. Following this, a buffer layer of silicon approximately 20 nm thick, is grown on the wafer which provides a clean, flat surface upon which to grow, as evidenced by reflection high energy electron diffraction (RHEED). A well-ordered template of MnSi(111) upon which to grow is necessary for a single-crystal growth. In order to produce this template, a 0.5 nm layer of amorphous Mn was deposited on the Si(111) surface and subsequently annealed at 400°C for one hour.

Then manganese and silicon were deposited at 400°C until a film thickness of 26.7 nm of material was reached. The film quality can then be checked with RHEED. A cap of silicon of approximately 20 nm was deposited in order to prevent oxidation of the MnSi film.

Both MnSi and Si are cubic crystals. Because of this, a slice through the (111)-plane produces a hexagonal surface lattice. This can be easily demonstrated by taking the dot product between two equivalent normalized lattice vectors that lie in the (111)-plane. For example $[1\bar{1}0]\cdot[10\bar{1}] = \cos\theta = 1/2$, which implies that these unit vectors have a 60° angular difference. For thin film MnSi on Si(111) substrates, it is in fact the case that the most energetically favourable orientation has $[1\bar{1}0]$MnSi(111)$\|[2\bar{1}\bar{1}]$Si(111). In other words, the [111]-directions are parallel but their $[1\bar{1}0]$-directions are offset by 30°. This orientation is shown in fig. 2.2, where the triangular shape of the material illustrates the three-fold rotational symmetry operator that runs about the [111]-axis.

The lattice constant for MnSi and Si are $a_{MnSi} = 0.4561$ nm and $a_{Si} = 0.5431$ nm, respectively. Despite the larger Si lattice, the surface cell for Si is actually smaller than that of MnSi. This is because of the diamond cubic structure of Si and the
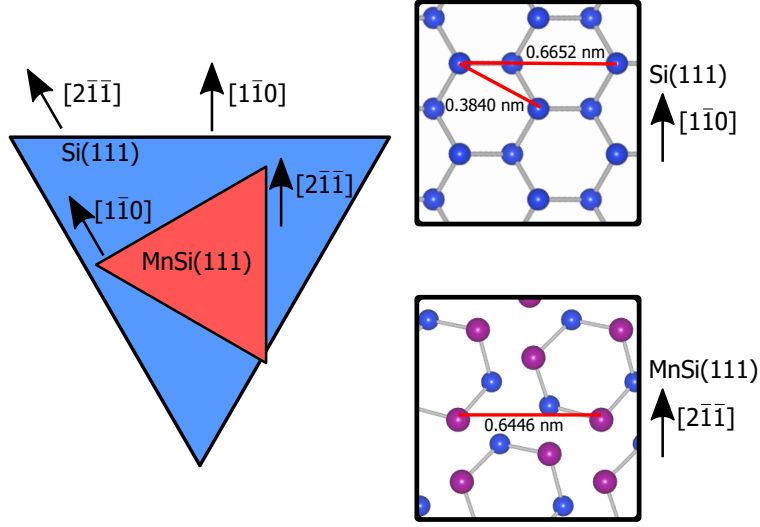
Figure 2.2: The surface lattices of MnSi(111) and Si(111) are such that the smallest epitaxial mismatch has MnSi(111) rotated 30° relative to underlying Si(111) substrate. The triangles represent the threefold symmetry operator that runs about the film normal.

fact that the cubic cell commonly used to describe diamond structures actually has a smaller primitive cell. The primitive surface lattice vector for MnSi corresponds to the $[1\bar{1}0]$ vector and has a magnitude of $\alpha_{MnSi} = \sqrt{2}a_{MnSi} = 0.645$ nm. The Si primitive surface lattice vector has a length of $\alpha_{Si} = a_{Si}/\sqrt{2} = 0.384$ nm. Because the surface lattice is hexagonal, there will be another lattice point a distance $\sqrt{3}\alpha_{Si} = 0.665$ nm away from the origin pointing in the $[2\bar{1}\bar{1}]$ direction. This means that the MnSi lattice point of $[1\bar{1}0]$ is nearly coincident with a Si lattice point provided that the two crystals are rotated 30° relative to each other. This yields a surface lattice mismatch of $(\alpha_{MnSi} - \sqrt{3}\alpha_{Si})/\alpha_{MnSi} = -3.1\%$ that results in a tensile strain in the MnSi(111) film.

2.1.3   MnSi/SiC

The SiC(0001) wafers grown upon were 300 μm thick and provided by PAM-XIAMEN. These wafers were cleaned in an ultrasonic bath of first acetone and then methanol. The native oxide of SiC was removed by depositing 1 nm of Si and then annealing at 1200°C. The SiO$_2$ layer can be removed in this way, leaving a clean SiC surface as

evidenced by RHEED [63][50].

We found that B20 MnSi would not form when manganese was in direct contact with the SiC substrate, because of this we adapted a technique initially developed by Higashi et. al [26]. A quadrilayer (QL) is a natural unit of thickness for MnSi(111) and refers to a 0.263 nm thick film of 2 dense and 2 sparse layers[27]. Though Higashi found that for films grown on Si(111) a 2 QL template was best, we found that by increasing the template to a thickness of 3 QL produced markedly better films. An amorphous 0.2 QL Si/1.5 QL Mn/1.3 QL Si/SiC(0001) trilayer was found to produce the smoothest film after annealing at 500 °C. Codeposition on top of this template was able to yield B20 MnSi films, although the growth produced complicated structures.

6H-SiC is a hexagonal crystal with an in-plane lattice constant of $a_{SiC} = 0.3073$ nm. This means that a super cell composed of four (2×2) SiC surface unit cells will be very close in size to a single surface unit cell of MnSi. The mismatch will be given by, $(\alpha_{MnSi} - 2a_{SiC})/\alpha_{MnSi} = +4.7\%$. This has a sign opposite to that of MnSi, indicating that any strain due to mismatch should be compressive in nature. The size of the lattices and orientations are shown in fig. 2.3. The triangle indicates the three-fold symmetry of the MnSi surface unit cell and the hexagon indicates the six-fold symmetry of the SiC surface. The fact that the underlying substrate has a six-fold rotational symmetry compared to the three-fold in MnSi, means that for every orientation there will be a degenerate orientation that has been rotated by 60° relative to the underlying substrate.

Though the orientation $[1\bar{1}0]$MnSi(111)$\|[10\bar{1}0]$SiC(0001) does have a small mismatch, there are other possible orientations with small mismatches. Determining the energetics of particular orientations is complicated, but orientations that are likely to occur can be estimated through the use of near-coincidence site lattice (NCSL) theory [28][46]. NCSL parametrizes epitaxial orientations with two quantities, the mismatch, δ and the ratio of total lattice sites to lattice sites that are nearly coincident with a lattice site on the substrate, Σ. In order to evaluate these quantities a translation vector for MnSi, $\vec{T}_{MnSi}(k,l) = k\vec{\alpha}_1 + l\vec{\alpha}_2$, must be chosen as well as a
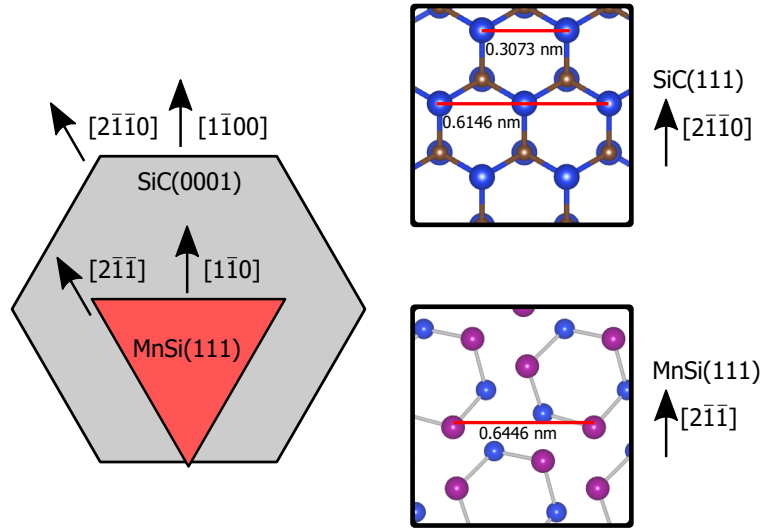
Figure 2.3: The MnSi(111) surface lattice is such that the expected favourable orientation has $[1\bar{1}0]$MnSi(111)$\|[1\bar{1}00]$SiC(0001). The triangle for the MnSi represents the threefold rotational symmetry axis that runs parallel to the film normal. The hexagon represents the sixfold axis that runs parallel to the film normal in SiC. This means that for any given orientation of MnSi with respect to SiC there will be a degenerate orientation that has been rotated 60° relative to the underlying substrate.
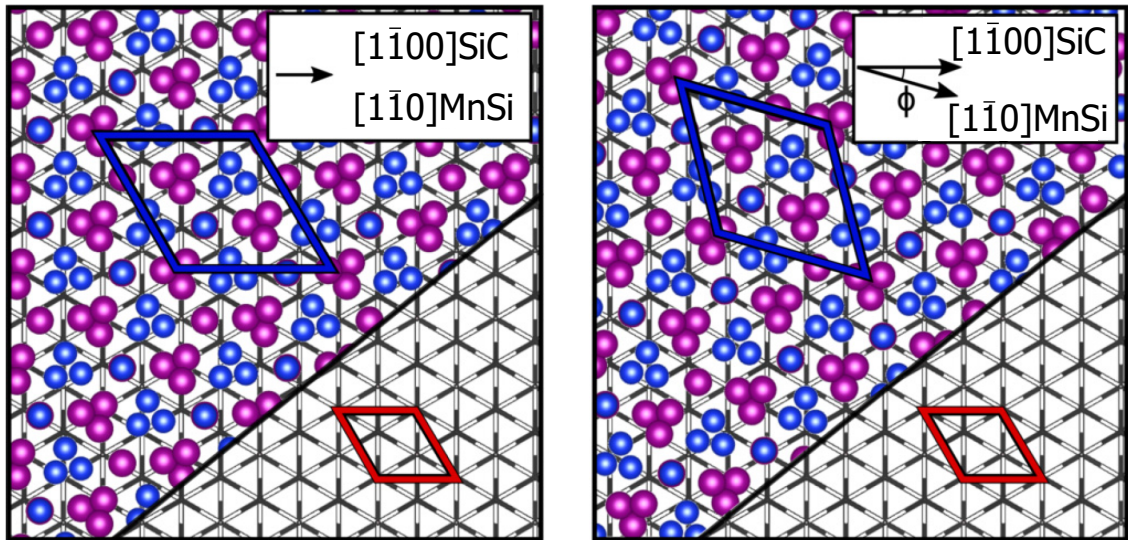
Figure 2.4: The MnSi(111) lattice can be rotated with respect to the underlying SiC lattice. The angle, ϕ, used in this thesis is defined by the angle between $[1\bar{1}00]$SiC and $[1\bar{1}0]$MnSi.

translation vector for SiC, $\vec{T}_{SiC}(m,n) = m\vec{\beta}_1 + n\vec{\beta}_2$. The primitive interfacial lattice vectors for MnSi correspond to $[1\bar{1}0]$ and $[01\bar{1}]$ translations and will be denoted as $\vec{\alpha}_1$ and $\vec{\alpha}_2$. The SiC primitive interfacial lattice vectors correspond to the $[10\bar{1}0]$ and $[01\bar{1}0]$ translations, and will be denoted by $\vec{\beta}_1$ and $\vec{\beta}_2$. Choosing any two surface lattice points will give a mismatch,

$$\delta = 2\frac{|\vec{T}_{SiC}(m,n)| - |\vec{T}_{MnSi}(k,l)|}{|\vec{T}_{SiC}(m,n)| + |\vec{T}_{MnSi}(k,l)|}, \tag{2.7}$$

and for hexagonal lattices,

$$\Sigma = k^2 + l^2 + kl. \tag{2.8}$$

From the symmetries of MnSi and SiC and the presence of left and right handed domains, only angles between $0°$ and $30°$ are truly unique. A set of points are said to be nearly coincident if the mismatch δ is less than 10%. Orientations that meet this criteria are then ranked based on their value for Σ. The orientations with the lowest Σ_{MnSi} were $0°$ ($\delta = -0.046, \Sigma_{MnSi} = 1$), $16.1°$ ($\delta = -0.006, \Sigma_{MnSi} = 3$) and $30°$ ($\delta = 0.096, \Sigma_{MnSi} = 3$).

2.1.4 Reflection High Energy Electron Diffraction

Reflection high energy electron diffraction (RHEED) is a technique commonly used in MBE to infer *in-situ* information about the crystal structure of the sample. A beam of electrons impinge upon the surface at glancing incidence and their outgoing paths will be determined by conservation of crystal momentum and conservation of energy. This geometric construction is called the Ewald sphere. This technique is sensitive to only the surface atoms in part because of the glancing incidence geometry [51].

Figure 2.5 shows the Ewald sphere construction. Because of the effective 2D surface lattice, the reciprocal lattice appears as a series of rods in k-space. For elastic scattering, kinetic energy is conserved and so the scattered electron with wavevector $\vec{k}_f$ will have the same magnitude as the incoming electron, providing the constraint
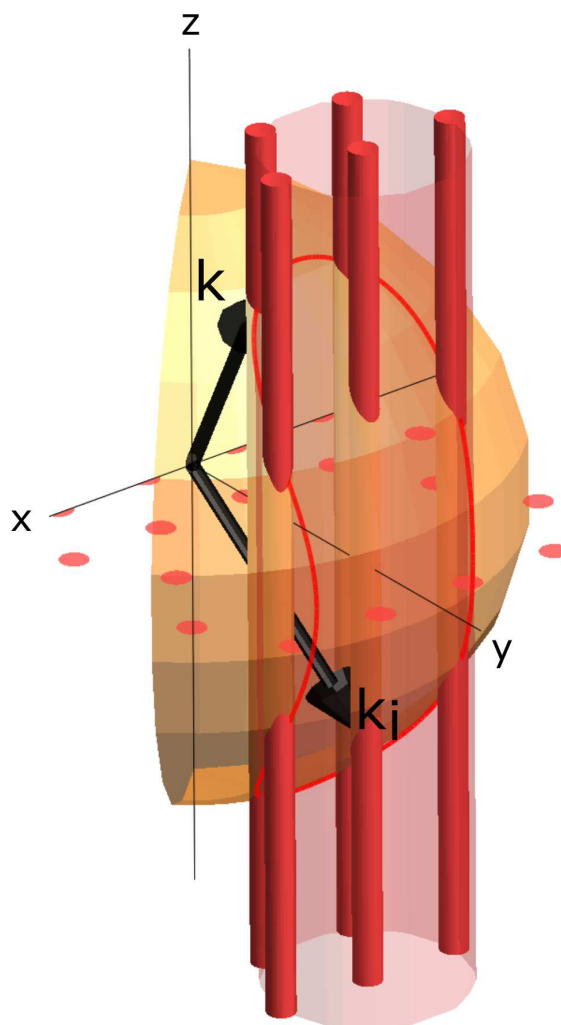
Figure 2.5: The Ewald sphere construction for determining scattering vectors in reflection high energy electron diffraction. Allowed scattering vectors for kinetically scattered electrons are determined by conservation of energy and conservation of crystal momentum. Vectors which satisfy conservation of energy lie on a sphere of radius $|\vec{k}_i|$. Vectors which satisfy conservation of crystal momentum will lie on reciprocal rods. The intersection of these two geometric objects will determine the possible scattering vectors for an electron.
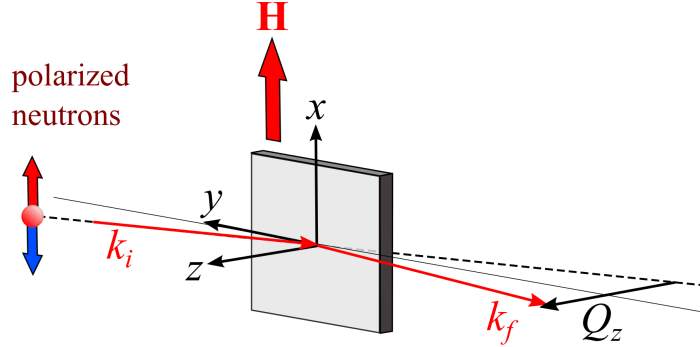
Figure 2.6: Experimental geometry for the PNR measurements presented in this thesis. The magnetic field and neutron spins are aligned along the x-direction. The neutrons impinge on the sample at glancing incidence, nearly parallel to the y-direction.

on the wavevectors, $|\vec{k_i}| = |\vec{k_f}|$. This forms a sphere in k-space and the intersection of this sphere with the reciprocal rods will provide the possible wavevectors for the scattered electron [51].

2.2   Neutron Reflectometry

PNR is a low incidence reflectometry technique that is sensitive to magnetic information and so it provides a useful means for extracting the magnetic texture of MnSi thin films. Because of the large size of the beam ($\sim$cm), PNR provides a depth profile of the magnetization averaged over the plane of the film[20]. Figure 2.6 shows the geometry used in our PNR measurements. The direction in which the magnetization is probed will be in the direction of the neutron spins, the x-direction for this experimental geometry [20].

The starting point for describing a neutron's wave function in PNR, $|\psi\rangle$, is the time-independent Schrödinger equation. Because neutrons are spin-1/2, the wave function can be expressed as a combination of spin-up and spin-down basis states, $|\psi\rangle = a_+ |+\rangle + a_- |-\rangle$. Solutions must be then found to,

$$[-\frac{\hbar}{2m_n}\nabla^2 + (V - E)]|\psi\rangle = 0, \tag{2.9}$$

where the energy of the neutron is,

$$E = \frac{\hbar^2 k_0^2}{2m_n} = \frac{4\pi^2 \hbar^2}{2m_n \lambda^2}, \tag{2.10}$$

where λ is the neutron wavelength. Scattered neutrons interact with the film through an effective potential that is the sum of both the nuclear contribution $(2\pi\hbar^2 \rho b/m_n)$ and the Zeeman contribution $(-\vec{\mu} \cdot \vec{B_{eff}})$. Here ρ is the atomic density, b is the coherent nuclear scattering length and B_{eff} is the effective magnetic field due to the magnetization within the layer. The effective potential is then,

$$V_{eff} = \frac{2\pi\hbar^2 \rho b}{m_n} - \vec{\mu} \cdot \vec{B_{eff}}. \tag{2.11}$$

The moment of a neutron is,

$$\vec{\mu} = g_n \mu_n \vec{\sigma}, \tag{2.12}$$

where $g_n = -1.9132$ is the Landé factor, $\mu_n = e\hbar/(2m_p) = 5.05 \times 10^{-27} J/T$ is nuclear magneton and $\vec{\sigma}$ is the Pauli operator associated with the neutron spin,

$$\sigma_x = \begin{pmatrix} 0 & 1 \\ 1 & 0 \end{pmatrix} \quad \sigma_y = \begin{pmatrix} 0 & -i \\ i & 0 \end{pmatrix} \quad \sigma_z = \begin{pmatrix} 1 & 0 \\ 0 & -1 \end{pmatrix}. \tag{2.13}$$

Because the potential in a film can be treated as one dimensional, the Schrödinger equation can be reduced to a one dimensional form. In order to understand the behaviour in a simple case, we can consider solutions for a homogeneous film with no external magnetic field. The Schrödinger equation will take the form of a Helmholtz propagation equation,

$$\frac{d^2\psi_z}{dz^2} + \frac{2m_n}{\hbar^2}(E - V)\psi_z = \frac{d^2\psi_z}{dz^2} + k^2\psi_z = 0. \tag{2.14}$$

This admits solutions of the form,

$$\psi_z = Ae^{ikz} + Be^{-ikz}. \tag{2.15}$$

We can relate the incident and transmitted wave-vectors through conservation of energy for both spin-up and spin-down eigenstates, and get,

$$(k_{tr}^{\pm})^2 = k_{in}^2 - 4\pi\rho b \pm \frac{2m_n g_n \mu_n}{\hbar^2}|B_{eff}|. \tag{2.16}$$

When the neutron enters the material, the kinetic energy is reduced by V and the wavevector will be reduced according to eqn. 2.16. In order to find the reflectivity coefficients we need to solve for the wave function within the material which we can do by satisfying the boundary conditions. Both the wave function and the derivative of the wave function with respect to z must be continuous across the interface. The incident wave function and the transmitted wave function will be of the form,

$$\psi_{z,in} = Ae^{ik_{in,z}z} + De^{-ik_{in,z}z} \tag{2.17}$$

$$\psi_{z,tr} = Ce^{ik_{tr,z}z} + De^{-ik_{tr,z}z}, \tag{2.18}$$

where $k_{in,z}$ and $k_{tr,z}$ are the z-components of the incident and transmitted wave-vectors. Satisfying the boundary conditions yields,

$$A + B = C + D \tag{2.19}$$

$$ik_{in,z}A - ik_{in,z}B = ik_{tr,z}C - k_{tr,z}D. \tag{2.20}$$

If we assume an infinite sample there is nothing for the transmitted wave to backscatter off of and $D = 0$. The transmission and reflection coefficients will be given by,

$$t = \frac{C}{A}, \quad r = \frac{B}{A}. \tag{2.21}$$
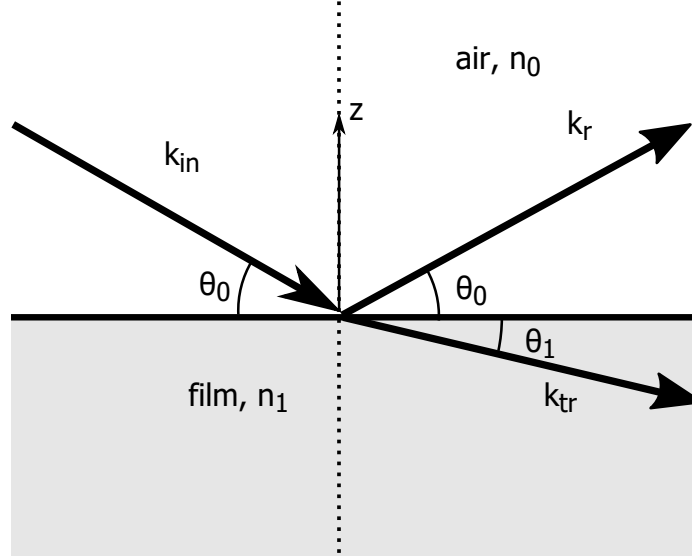
Figure 2.7: The angles of refracted and reflected scattering vectors for a neutron scattering off an interface.

With $R = |r|^2$ we obtain the reflectivity,

$$R = \left(\frac{k_{in,z} - k_{tr,z}}{k_{in,z} + k_{tr,z}}\right)^2. \tag{2.22}$$

Figure 2.7 shows the geometry of a neutron scattering off a film. The index of refraction will be given by $n = k_{tr}/k_{in}$. With this convention, the reflectivity can be expressed in the Fresnel form as,

$$R = \left(\frac{k_{in}\sin\theta_{in} - k_{tr}\sin\theta_{tr}}{k_{in}\sin\theta_{in} - k_{tr}\sin\theta_{tr}}\right)^2 = \left(\frac{\sin\theta_{in} - n\sin\theta_{tr}}{\sin\theta_{in} + n\sin\theta_{tr}}\right)^2. \tag{2.23}$$

Since the in-plane component of the wavevector is conserved, we get the relation,

$$k_{tr}\cos\theta_1 = k_{in}\cos\theta_0. \tag{2.24}$$

Using this we can get the reflectivity,

$$R = \left(\frac{\sin\theta_0 - \sqrt{n^2 - \cos^2\theta_0}}{\sin\theta_0 + \sqrt{n^2 - \cos^2\theta_0}}\right)^2. \tag{2.25}$$

The critical angle for total reflection occurs when $\theta_1 \to 0$. For small angles, we will get

$$1 - \theta_c^2/2 = 1 - \frac{4\pi\hbar^2\rho b \pm 2m_n g_n \mu_n |B_{eff}|}{\hbar^2 k_{in}^2}, \tag{2.26}$$

$$\to \theta_c = \frac{\sqrt{4\pi\hbar^2\rho b \pm 2m_n g_n \mu_n |B_{eff}|}}{\hbar k_{in}}. \tag{2.27}$$

This means that a neutron scattering experiment can determine the effective field within a magnetized sample just by comparing the difference in critical angles between spin-up and spin-down neutrons. This can be useful in cases where contaminants or the film substrate are interfering with other bulk magnetization measurement techniques, such as SQUID magnetometry.

We can write the reflectivity in terms of the critical angle. Because $\cos\theta_c = n$, we can rewrite eqn. 2.25 in the limit of small angles as,

$$R = \left(\frac{1 - \sqrt{1 - (\theta_c/\theta_0)^2}}{1 + \sqrt{1 - (\theta_c/\theta_0)^2}}\right)^2, \tag{2.28}$$

which in the limit of $\theta_c/\theta_0 \approx 0$ will yield,

$$R = \frac{\theta_c^4}{16\theta_0^4}. \tag{2.29}$$

This leads to a very quick reduction in intensity as the angle is increased and is the reason for the very sharp drop in the intensity of neutron reflectivity experiments as the angle is increased. For a multilayer film the analysis is somewhat more difficult as D will not be equal to 0. For a multilayer film, multiple reflections can occur between layers. In order to treat this it's necessary to propagate the wave through and account for the fact that the wave can be transmitted or reflected at each interface.

This leads to fringes in the reflectivity and can complicate the analysis. The width of these fringes is correlated with the thickness of the layers in the multilayer film.

In general, modelling reflectivities is difficult when dealing with a complicated sample composed of multiple materials and layers. A typical model will usually have thickness, interfacial roughness, densities, b and the size of the magnetic moment as fitting parameters. The values of these parameters can be estimated but aren't precisely known. In these cases, the parameter space is sufficiently large that numerical modelling software such as SIMULREFLEC, is needed to calculate the multiple reflections and fit material parameters. The parameter space is explored and χ^2 is numerically minimized. The parameters (except for the magnetic moment) are fit independently through a combination of X-ray reflectivity (XRR) and XRD [35]. The magnetic fit parameters such as H_D are fit through a least squares method and further constrained through SQUID measurements.

SIMULREFLEC is used to fit the PNR data. The shape of the reflectivity data gives information about the chemical and magnetic structure but by analysing the difference between the spin-up and spin-down channels we can obtain a signal that is very sensitive to the depth distribution of spins within the sample. PNR measurements sample over a comparatively large area determined by the beam size and so a magnetic profile averaged along the in-plane directions can be obtained. The resolution in the depth of the film is much better and is primarily limited by the neutron wavelength, $\lambda_n = 0.237$ nm. The polarized neutron reflectometry (PNR) measurements shown in this thesis were conducted at the Canadian Nuclear Laboratories [75].

2.3 Electrical Measurements

Electrical measurements were performed on a Quantum Design Physical Properties Measurement System (PPMS) on films that had been capped with a 20 nm protective amorphous Si layer. Samples were photolithographically patterned into a four-probe geometry as shown in fig. 2.8. Gold wires leads were attached to sample with indium solder. The samples were patterned using SPR220 3.0 photoresist and were etched
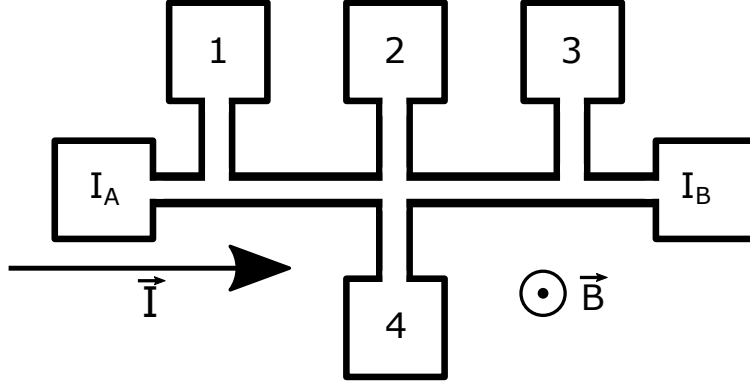
Figure 2.8: Photolithographically patterned geometry for electrical measurements on MnSi/SiC. The voltage difference between pads 1 and 3 will be proportional to ρ_{xx}. The voltage difference between 2 and 4 will be proportional to ρ_{yx}.

with a 2-keV Ar-ion gun [49][46].

Figure 2.8 shows the geometry of the PPMS pattern. The longitudinal voltage will be given by $V_{xx} = V_3 - V_1$, where V_i refers to the voltage at the ith pad. The Hall voltage will be given by $V_{yx} = V_4 - V_2$. The longitudinal resistivity is given by

$$\rho_{xx} = \frac{V_{xx}wt}{IL},\tag{2.30}$$

where $w = 0.5$ mm is the width of the pattern, $L = 10$ mm is the distance along the Hall bar where the voltage is measured, t is the film thickness and I is the current. The Hall resistivity is defined as

$$\rho_{yx} = \frac{V_{yx}t}{I}.\tag{2.31}$$

The Hall effect in magnetic materials is usually broken up into three terms, the ordinary $\rho_{yx}^O = \mu_0 R_0 H$, the anomalous[61][4][36] ρ_{yx}^A and the topological [53] ρ_{yx}^T Hall effects. The anomalous Hall effect is usually broken up into intrinsic and extrinsic terms. In addition conical magnetic textures require an additional term, ρ_{yx}^{other}, that arises from scattering in a conical structure [49]. The total Hall effect will be,

$$\rho_{yx} = \rho_{yx}^O + \rho_{yx}^{A,int} + \rho_{yx}^{A,ext} + \rho_{yx}^T + \rho_{yx}^{other}.\tag{2.32}$$

35

The extrinsic term, $\rho_{yx}^{A,ext} = \alpha\rho_{xx}M + \beta\rho_{xx}^2 M$ is composed of skew scattering [61] parametrized by α, and side-jump scattering [4] parametrized by β. The intrinsic term is given by the following expression, $\rho_{yx}^{A,int} \sim \rho_{xx}^2 M$ [36]. Because the intrinsic and side-jump are very difficult to separate, they are grouped into one term, $\rho_{yx}^{int,sj} = b(T)\rho_{xx}^2 M$. Because of these dependences a first-order phase transition could be observed. A discontinuity in the field dependence of the resistance could be observed if the films have a transition between phases. The Hall resistance should also exhibit a discontinuity if there is a phase transition. One of the components in the Hall effect is the topological Hall effect (THE) and is a component that arises from a geometric phase factor called the Berry phase [7]. This factor comes about when an electron adiabatically follows the local magnetization of a field with non-trivial topology. This phase results in a transverse velocity which can be expressed in terms of an effective magnetic field, $B_{eff} = n_s(h/e)$, where n_s is the skyrmion number density,

$$n_s = \frac{1}{4\pi}\hat{m} \cdot \left(\frac{\partial\hat{m}}{\partial x} \times \frac{\partial\hat{m}}{\partial y}\right), \tag{2.33}$$

which is the integrand of eqn. 1.11. The THE then takes on a form similar to the regular Hall effect, although a term proportional to the polarization, P needs to be added because electrons with opposite spins acquire opposite phases. The THE due to skyrmions is,

$$\rho_{yx}^T \cong PR_0 B_{eff}. \tag{2.34}$$

The longitudinal resistance, or magnetoresistance (MR) also provides insight into the magnetic texture of the films [49]. Peaks in the second derivative of the MR have been shown to correlate with changes from a conical state to a ferromagnetic state. Electrical measurements can thus provide key evidence in determining the prominent magnetic phase of our films.

2.4 Computational Methods

MUMAX3, a Go-based GPU-accelerated micromagnetic package [70], was used throughout the analysis of the PNR data to predict the spin distribution in these MnSi thin films. In order to find the lowest energy state a steepest gradient descent algorithm was used within the MUMAX3 framework. Steepest gradient minimization relies on the system being close to the minimum energy and so the initial conditions before energy minimization are critically important.

The essential idea in gradient descent minimization is to reduce the function that is to be minimized (in this case energy), in the direction opposite to the largest gradient. Say we are minimizing the function $F(\vec{x})$, starting at the point $\vec{x}_i$. The subsequent point will be chosen such that,

$$\vec{x}_{i+1} = \vec{x}_i - \tau_i \nabla F(\vec{x}_i), \tag{2.35}$$

where τ_i is an appropriately chosen step size which should be allowed to change each iteration. This method is an iterative algorithm which probes the function only in the vicinity close to a point x_i.

The specific micromagnetics energy minimization scheme chosen was the Exl method [17], which is a modification of the Barzilai-Borwein method [3]. The algorithm searches for the lowest free energy, $F(\hat{m})$, on a sphere. The method used in MUMAX3 does not keep the magnetization constant and so must be renormalized after each step. Step directions are chosen such that,

$$\vec{m}_{i+1} = \hat{m}_i - \tau_i \hat{m}_i \times (\hat{m}_i \times \nabla F(\hat{m}_i)). \tag{2.36}$$

After this step, the magnetization is normalized with $\hat{m}_{i+1} = \vec{m}_{i+1}/|\vec{m}_{i+1}|$ and the iteration repeats. Step sizes are chosen by alternating between τ_i^1 and τ_i^2 where these are given by,

$$\tau_i^1 = \frac{(\hat{m}_i - \hat{m}_{i-1})^2}{(\hat{m}_i - \hat{m}_{i-1}) \cdot (\hat{m}_i \times (-\hat{m}_i \times \nabla F(\hat{m}_i))} \tag{2.37}$$

and,

$$\tau_i^2 = \frac{(\hat{m}_i - \hat{m}_{i-1}) \cdot (\hat{m}_i \times (-\hat{m}_i \times \nabla F(\hat{m}_i)))}{(\hat{m}_i \times (-\hat{m}_i \times \nabla F(\hat{m}_i))^2}. \tag{2.38}$$

These step sizes are chosen according to the Barzilai-Borwein criteria [3] and are solutions to $\tau = \min_{\mathrm{arg}}[F(\vec{x}_i + \tau \nabla F)]$. The energy is calculated using a finite difference discretization of space using an orthorhombic grid of nearly cubic cells. Periodic boundaries are used in x and y directions except where indicated otherwise. For the exchange interaction, the effective field is calculated using a 6-neighbour small-angle approximation,

$$\vec{B}_{exch} = 2 \frac{A_{ex}}{M_{sat}} \sum_i \frac{\hat{m}_i - \hat{m}}{\Delta x^2}. \tag{2.39}$$

Derivatives arising from DMI, are handled as central derivatives,

$$\frac{\partial \vec{m}_i}{dx} = \frac{\vec{m}_{i+1} - \vec{m}_{i-1}}{2\Delta x}. \tag{2.40}$$

It is important to have sufficiently small cell sizes in order to avoid discretization errors. Generally it was found that artefacts can be avoided if angular separation between neighbouring cells is less than $10°$ (in reality the size of the artefacts will be related to the second derivative of angle in space). Given that the helical wavelength in thin film MnSi is ≈ 14 nm, this puts an upper limit on cell size of 0.4 nm. A cell size of 0.1 nm was used for most of the simulations.

Chapter 3

Magnetic Phases of MnSi/Si(111) with In-Plane Fields

In this chapter I will discuss the work that was done on MnSi/Si(111) samples in order to demonstrate the existence of in-plane (IP) skyrmions and to resolve the controversy regarding the phase diagram in fig. 1.6. The stars in this phase diagram correspond to the fields discussed in this chapter. We used polarized neutron reflectometry (PNR) in combination with computational modelling techniques to put forward evidence that IP-skyrmions are an energetically favourable magnetic state in MnSi/Si(111) thin films with an applied IP magnetic field of $\mu_0 H = 0.5$ T, at a temperature of 25 K. Evidence supporting two other phases is presented. A twisted ferromagnetic phase is found at $\mu_0 H = 0.7$ T and a distorted skyrmion phase is found at $\mu_0 H = 0.3$ T. The results are notably different than those found in ref. [73], which present results for in-plane fields at $T = 5$ K that show the system exists definitively in a helicoidal state.

The magnetic field was applied along the MnSi[$1\bar{1}0$] direction or the x-direction as shown in fig. 2.6. The samples were first cooled in a magnetic field of $\mu_0 H = 0.8$ T from $T = 100$ K to $T = 25$ K. PNR measurements were performed after decreasing the magnetic field to the target at a constant temperature of $T = 25$ K. Using a combination of MUMAX3 and SIMULREFLEC we can predict magnetic depth profiles and calculate the expected reflectivity using SIMULREFLEC.

3.1 The Twisted Ferromagnetic State

At high magnetic fields, such as $\mu_0 H = 0.7$ T, the system exists in a nearly saturated state where most of the magnetic modulation is suppressed but small twists exist at the surfaces [73][47]. This is called the twisted ferromagnetic state and is shown in fig. 3.1. This shows the lowest energy state for a film with $\mu_0 H_D = 0.85$ T, $L_D = 13.9$ nm
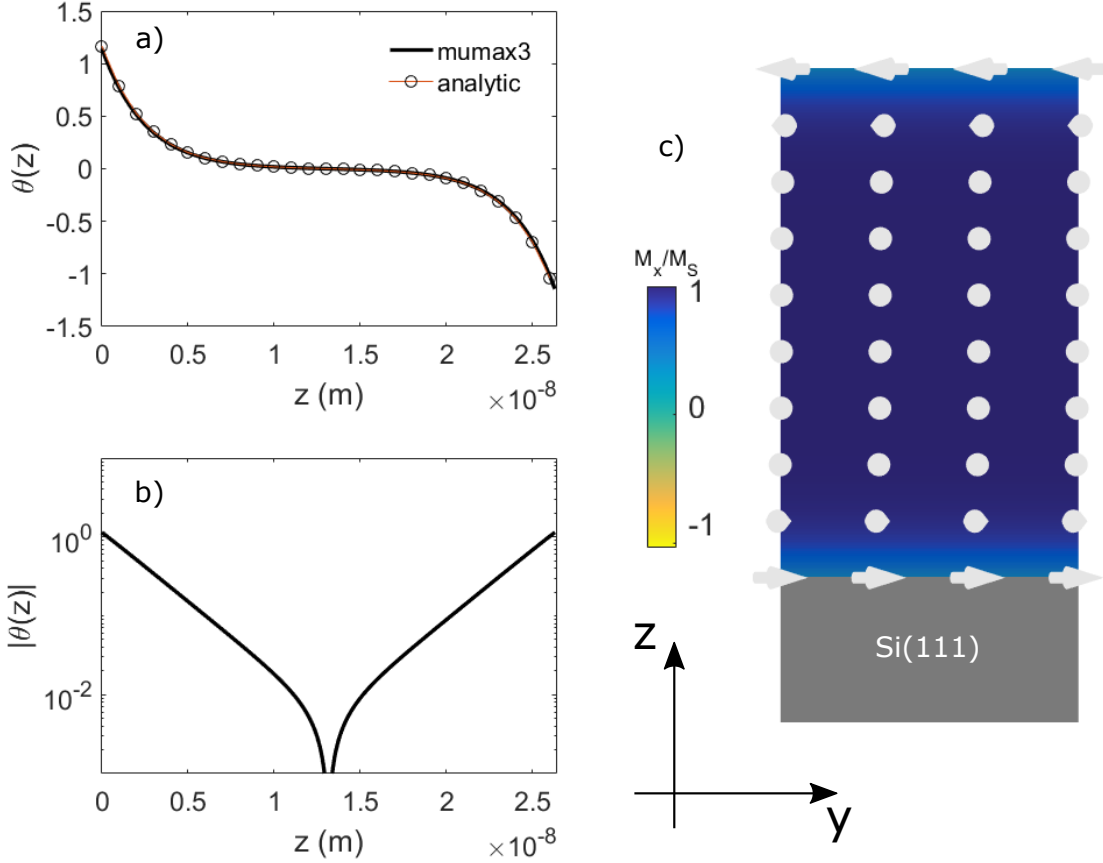
Figure 3.1: The twisted ferromagnetic state is composed of a nearly ferromagnetic centre with approximately exponentially decaying angles. The computationally calculated angle as a function of position is shown in a), this is compared to the analytic solution derived in ref. [47].

and $M_S = 138 \, \text{kA/m}$. SQUID measurements have demonstrated that for high enough IP fields the system will exist in a twisted ferromagnetic state. Near the centre of the film the system is nearly completely ferromagnetic with the spins aligned along the field direction. However, near the edges due to the lack of pinning at the surfaces the spins naturally form a twisted structure. These twists play an important role in the trapping and confinement of skyrmions [47] as they provide an energy barrier to the annihilation of skyrmions from the film boundaries.

In ref. [47] an analytic form is derived for this state. We assume a film with the normal pointing along z and the applied field pointing along the x-direction. We use a one-dimensional modulation of the magnetization that depends only on z with

no out-of-plane (OOP) component due to the anisotropy. The magnetization will be given by $\vec{M} = M_S[\cos(\theta(z)), \sin(\theta(z)), 0]$ and substituting this into eqn. 1.1, we arrive at the one-dimensional energy functional,

$$F = \int_{area} \int_0^\infty [A(\frac{d\theta}{dz})^2 - D\frac{d\theta}{dz} + \mu_0 H M_S (1 - \cos\theta)] dz dA, \qquad (3.1)$$

where $\theta(z)$ is the angle with respect to the external field. Using the boundary conditions $\theta(0) = 2\arcsin\sqrt{H_D/(4H)}$ and $\theta(\infty) = 0$ [47]. Minimization of the free energy functional yields the solution,

$$\theta(z) = 4\arctan[C(H)\exp(-2\pi z\sqrt{H/H_D}/L_D)], \qquad (3.2)$$

where,

$$C(H) = 2\sqrt{H/H_D} - \sqrt{4(H/H_D) - 1}. \qquad (3.3)$$

The analytic solution is plotted with the computational solution in fig. 3.1 a). There is no appreciable difference between these solutions and this provides an important check on the reliability of the computational results. Figure 3.1 b) shows that this solution is very nearly exponential.

In order to find the ground state distribution of spins for this twisted ferromagnetic state, we use MUMAX3 to model a system of 4096x256 spins of dimensions 420.8 nm in the y-direction by 26.3 nm in the z-direction. The x direction is 1 cell and has periodic boundary conditions applied. The y direction also has periodic boundaries. The parameters of $\mu_0 H_D = 0.85$ T, $M_S = 138kA/m$ were used.

Two key parameters in modelling the magnetization are the strength of the exchange energy, A, and the strength of the DMI, D. These can in principle be extracted from the measurement of the helical wavelength $L_D = 4\pi A/D$ and the saturation field $\mu_0 H_D = D^2/(2AM_S)$ but in practice, for IP fields, the nearly ferromagnetic state never fully saturates due to the twisting at the surfaces which complicates the

Layer	Thickness (nm)	Density ($\times 10^{28}$ m^{-3})	b (fm)	σ (nm)
Si substrate	∞	5	4.2	0
MnSi	26.3	8.4	0.2	0
MnSi+Si	0.4	6.9	0.6	0.27
SiO$_2$	1.8	5.3	4.2	0.77
a-Si	20.6	1.8	15.8	0.55

Table 3.1: Material parameters for polarized neutron reflectometry (PNR) as obtained through a combination of X-ray reflectivity and PNR in ref. [35][75]. MnSi+Si represents a thin silicon rich MnSi phase that exists near the film interfaces.

measurement of H_D. To estimate H_D, it is usually easiest to measure the magnetization for OOP fields where the surface twists are essentially absent. However, due to the demagnetizing field we can only obtain the sum, $\mu_0 H_D + \mu_0 H_u = 0.86$ T.

Superconducting quantum interference device (SQUID) magnetometry measures the magnetization as a function of $\mu_0 H$ and T as averaged over the whole of the film. For OOP fields the magnetization is linear up until saturation, which rules out the possibility of out-of-plane skyrmions [34]. The boundary of any skyrmionic phase would appear as a peak in the derivative of the magnetization with respect to the applied field, a feature which is not observed. These measurements constrain $H_u < 0$ and so we have the constraint $\mu_0 H_D \leq 0.86$ T.

Figure 3.2 a) shows the reflectivity as a function of the scattering vector for spin-up and spin-down neutrons. The nuclear portion of the reflectivity was determined by X-ray reflectometry and neutron reflectometry measurements above the ordering temperature [35][75]. The nuclear parameters used in fitting are presented in table 3.1 where b is nuclear scattering length and σ is the root-mean squared layer roughness. A thin Si-rich MnSi phase was found near the film interfaces and is shown by the MnSi+Si layer.

The spin asymmetry, $(R_+ - R_-)/(R_+ + R_-)$, is a convenient quantity for visualizing the effect of the magnetic structure. Because this quantity is proportional to the difference in spin-channels, the magnetic contribution to the scattering is highlighted whilst the nuclear contribution is largely removed. The reflectivity for fields of 700 mT is shown in fig. 3.2 a) and the spin asymmetry is shown in b). The value of
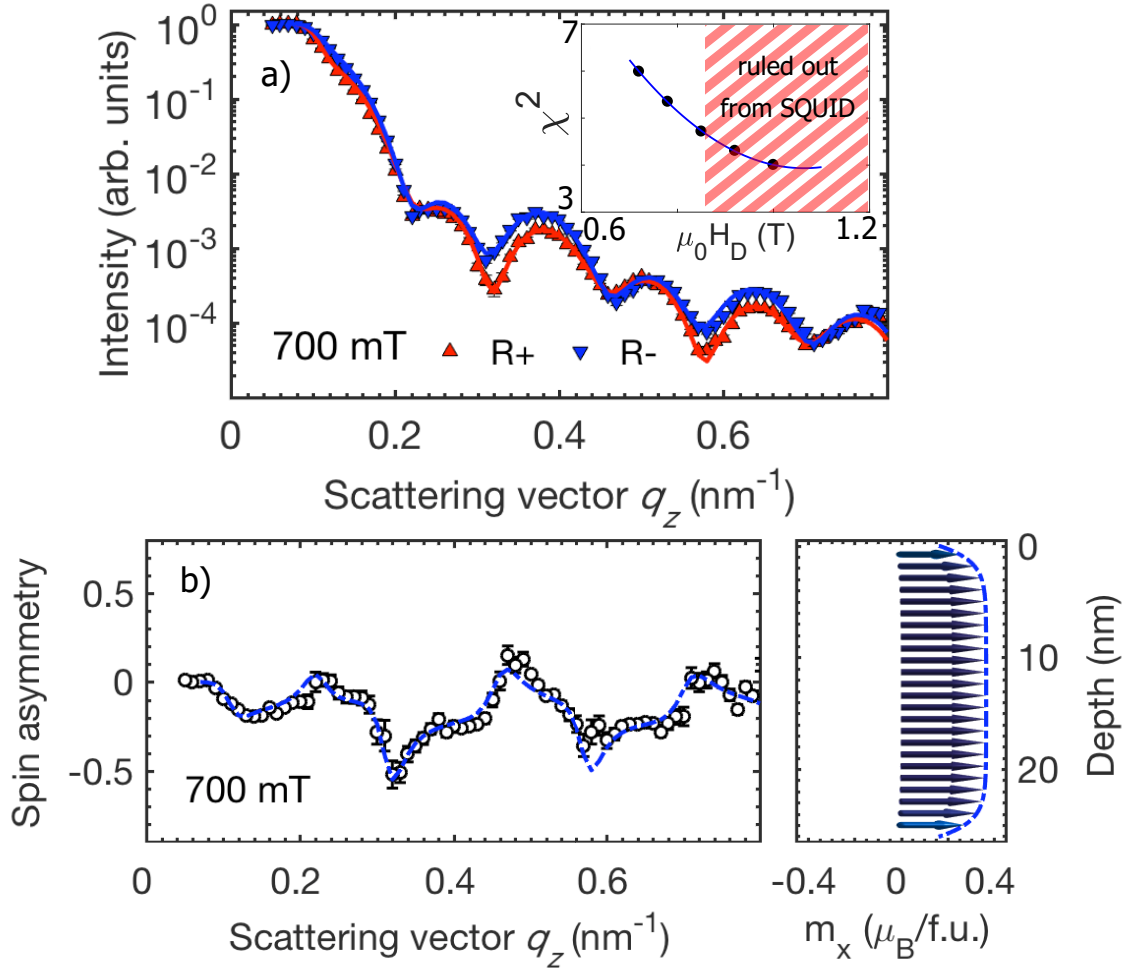
Figure 3.2: The reflectivity as a function of scattering vector, q_z, is shown in a) for fields of $\mu_0 H = 700$ mT. The inset shows χ^2 as a function of H_D which was used as a fit parameter. The spin asymmetry is mostly due to the magnetic structure of the film. On the right, the depth profile used for the best fit is shown.

H_D was fit for the fields of 700 mT where in-plane modulations are suppressed. For the twisted ferromagnetic state, H_D is effectively the only fitting parameter and so, with the constraints provided by SQUID magnetometry, we arrive at a reasonable estimate. The inset of figure 3.2 shows χ^2 as a function of H_D for fields of 700 mT. It was found that $\mu_0 H_D = 1.06 \pm 0.26$ T where the error-bars correspond to deviations in χ^2 of ± 1. Because the lack of OOP skyrmions constrains $H_u < 0$, the best fit for H_D is estimated to be $\mu_0 H_D = 0.85$ T. This constraint is represented by the red hatched region.

Figure 3.3 shows the spin asymmetry for the 700 mT data and a fit denoted by the red line that uses the best value of H_D. The blue line shows a fully saturated model without the surface twists and is inconsistent with the spin asymmetry. Despite their relatively small spatial extent, this shows the importance of these surface twists in fitting the data and gives an indication of the sensitivity of PNR to small magnetic modulation. With the surface twists understood and a reliable estimate of H_D obtained, it is then possible to fit the more complicated structures that emerge at lower fields.

3.2   In-Plane Skyrmions

For 500 mT, there is evidence from previous magnetometry measurements in ref. [74] that an additional magnetic phase exists that is not present at lower temperatures. However, Yokouchi *et al.* [76] claim that these films exist in a purely helicoidal state. It is worth noting that these measurements are performed while reducing the field and so we are comparing magnetic states for decreasing magnetic fields only.

PNR measurements were then performed at $\mu_0 H = 500$ mT and $T = 25$ K as this was determined to be in the centre of the skyrmionic phase as shown in the phase diagram in fig. 1.6. Yokouchi *et al.* [76] claim from planar Hall effect measurements that this region should not have skyrmions. These PNR measurements are probing this controversial region of the phase diagram. We compare fits obtained from using both a helicoidal and a skyrmionic phase.
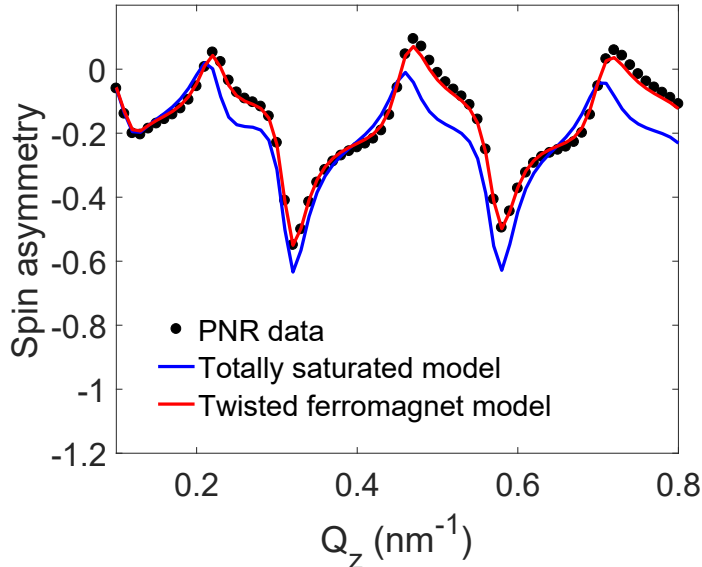
Figure 3.3: A comparison between the predicted spin asymmetry for a twisted ferromagnetic model and a simple ferromagnetic model. We can see that the twisted ferromagnetic model captures the features better than the a completely saturated model.

Figure 3.4 shows a comparison in the magnetic depth profile for these two states. The main difference in the depth profiles for these states is the fact that the moment in the centre of the film, $m_x(z = t/2) = -1$, for the helicoidal phase. In the skyrmion phase, the magnetic moments in the regions between skyrmions point parallel to the field and so the average moment in the centre of the film increases relative to the helicoidal phase. This difference leads to a noticeable change in the spin asymmetry for the two fits.

Using the value of $\mu_0 H_D = 0.85$ T obtained through fitting the twisted ferromagnetic state, skyrmionic systems were simulated. A system of equally spaced in-plane skyrmions was chosen as the initial state for the micromagnetic simulations. These skyrmions have their axes of symmetry pointing within the plane of the film and along the field direction. With H_D specified, the only fitting parameter is the spacing between the skyrmions, although this parameter can be calculated as well. This calculation can be performed by calculating the energy for a skyrmion lattice and minimizing with respect to spacing. We chose 256 cells along the z-direction and 4096
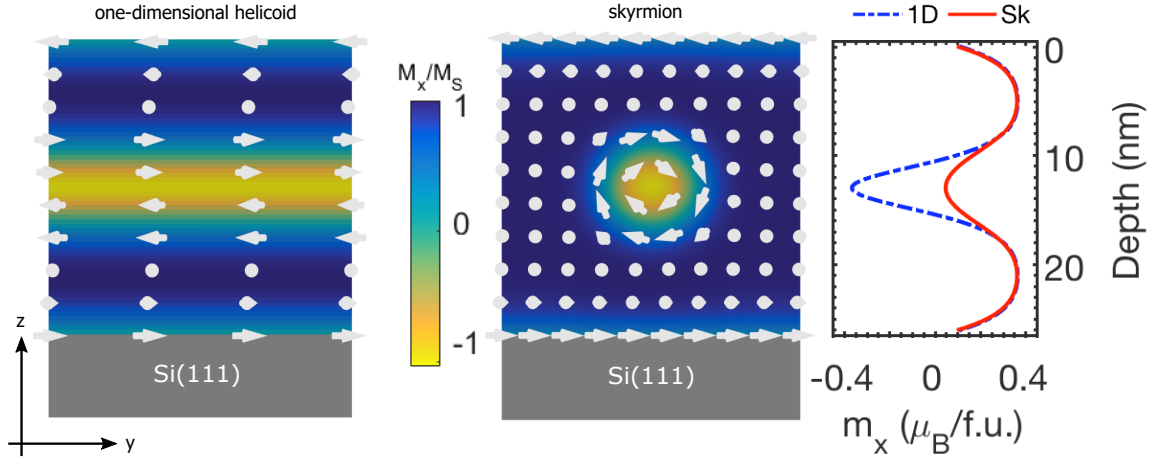
45

Figure 3.4: A comparison between the magnetic depth profile for a one-dimensional model that has a single turn helicoid and a skyrmion. The major difference between these depth profiles is the average moment in the centre of the film. Because the skyrmion state has regions in the centre of the film that are ferromagnetic, the average moment for a skyrmion is higher in the film centre.

along the y-direction and 1 along the x-direction – corresponding to a 26.3×420.8 nm grid – with periodic boundaries along the x and y directions. An in-plane field of 0.5 T is applied along the x-direction.

By varying the number of skyrmions within the film, the spacing between the skyrmions, $L_{Dy} = L_y/N_{skyr}$, is varied. It is assumed that such a system of equally spaced skyrmions is close to the ground state distribution of a skyrmionic chain. Because skyrmions are topologically stable solitons, they cannot be destroyed without overcoming a significant energy barrier. This means that the number of skyrmions will remain constant throughout the steepest gradient energy minimization process. The equilibrium inter-skyrmion distance is found by calculating the energy as a function of the number of skyrmions in a fixed volume and was also fit.

Figure 3.7 a) shows the energy for a 26.3 nm (in the z-direction) by 420.8 nm (in the y-direction) thin film with periodic boundaries in the x- and y-directions as a function of skyrmion population. The z-direction has free boundaries. We can see that there is an equilibrium spacing that corresponds to 19.3 nm.

The intensity as a function of q_z for an in-plane skyrmion fit is shown in fig. 3.5 a). The magnetization depth profiles are calculated for a series of skyrmion densities.

These are input into SIMULREFLEC in order to calculate the neutron reflectivities and spin asymmetries. As the skyrmion spacing decreases, the magnetization in the centre of the films increases. The inset shows χ^2 for skyrmion fits as a function of the spacing between skyrmions. At fields of 500 mT we found $L_{Dy} = 22 \pm 7$ nm which is close to the value of 21 nm that was also found with small angle neutron scattering experiments. This is in good agreement with the micromagnetic calculations provided by MUMAX3 as discussed below.

The spin asymmetry for $\mu_0 H = 500$ mT is shown in fig. 3.5 b). Two fits are shown here to emphasize the fact that a helicoidal phase does not fit well with this data. The red line shows a fit obtained with a skyrmion profile and the blue line shows a fit obtained with a helicoidal profile which is noticeably worse. The PNR asymmetry provides strong evidence that the centre of the film has a moment which is larger than would be expected for a strictly one-dimensional helicoidal phase. The fact that the PNR is in strong agreement with the micromagnetic calculation provides strong evidence that the film exists in a skyrmionic state at this field value.

3.3   Skyrmion-Skyrmion Interactions

The interaction potential between skyrmions was investigated in the process of fitting the 500 mT data. Because of the confinement in our films, they present a convenient geometry for studying inter-skyrmion interactions for IP skyrmions. The energy of the calculation, E_{calc}, for a $L_x \times L_y \times t$ system with N skyrmions will be given by,

$$E_{calc}(N) = L_x(N(E_{skyr} + L_y E_{back} + N E_{int}(N))), \tag{3.4}$$

where E_{back} is the energy per unit area of the twisted-ferromagnetic background without any skyrmions and E_{skyr} is the energy per unit depth along x-direction required to add a skyrmion to this background. The ferromagnetic background scales with the area of the film and so normalizing the background energy by the area is the most natural approach. Since the skyrmion self-energy scales linearly with increasing L_x, it is natural to report skyrmionic energies normalized by the length of the skyrmion in
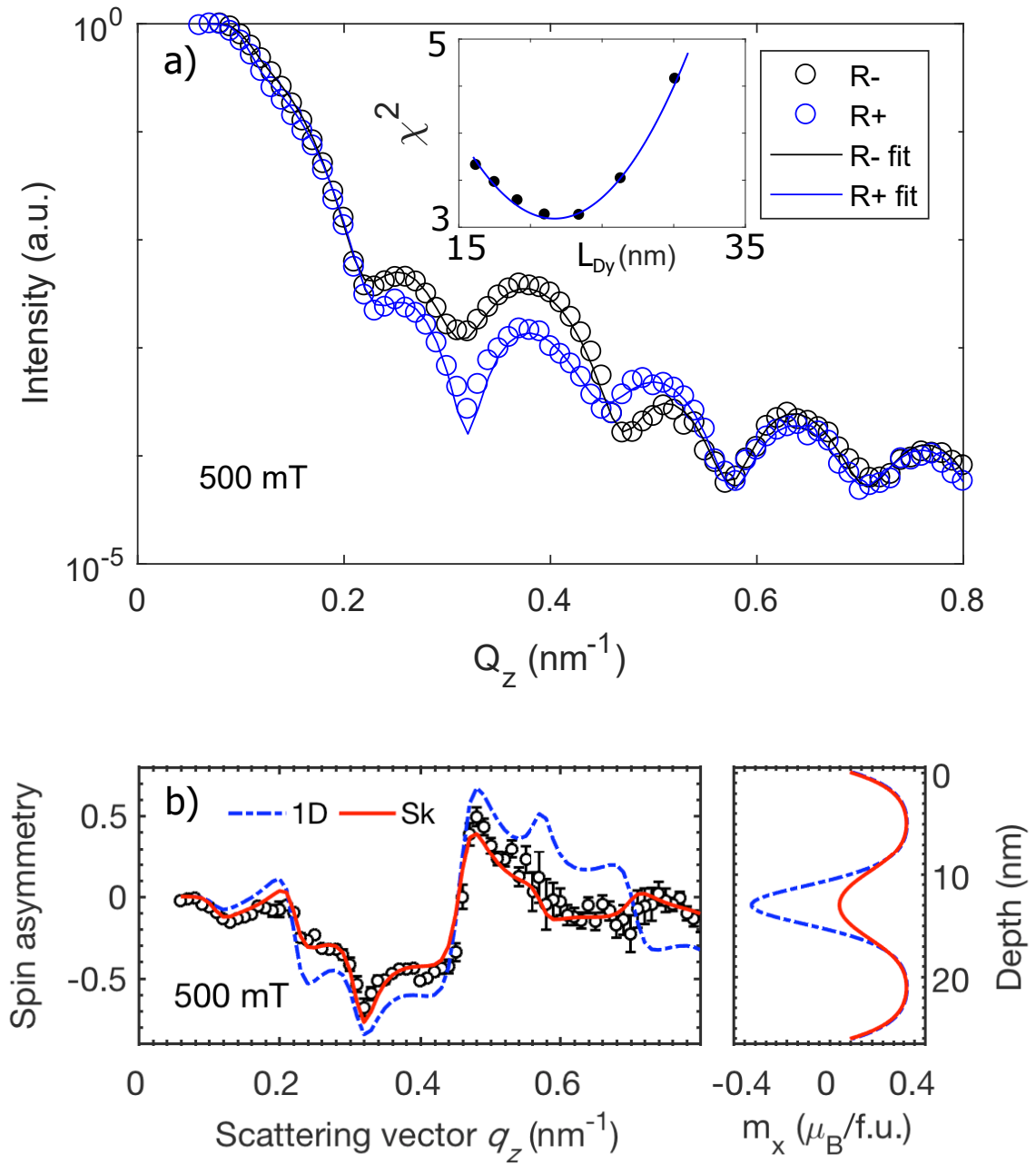
Figure 3.5: PNR reflectivity for a field of $\mu_0 H = 500$ mT is shown in a). The inset shows χ^2 as a function of the fit parameter, L_{Dy}, which corresponds to the skyrmion spacing. The spin asymmetry for 500 mT data is shown in b). The blue dotted line is the fit for a 1D helicoid and the red dotted line is the fit for a skyrmionic state. The PNR data supports the hypothesis that a skyrmionic state is present for this field. The fitted skyrmion separation was found to be $L_{Dy} = 22 \pm 7$ nm which is consistent with SANS and micromagnetic calculations.

Figure 3.6: The energy for a system of length $L = 420.8$ nm as a function of the number of skyrmions in the system. For low densities, the functional form is a line with a slope equal to the skyrmion self-energy. The intercept is the energy density of the ferromagnetic background.

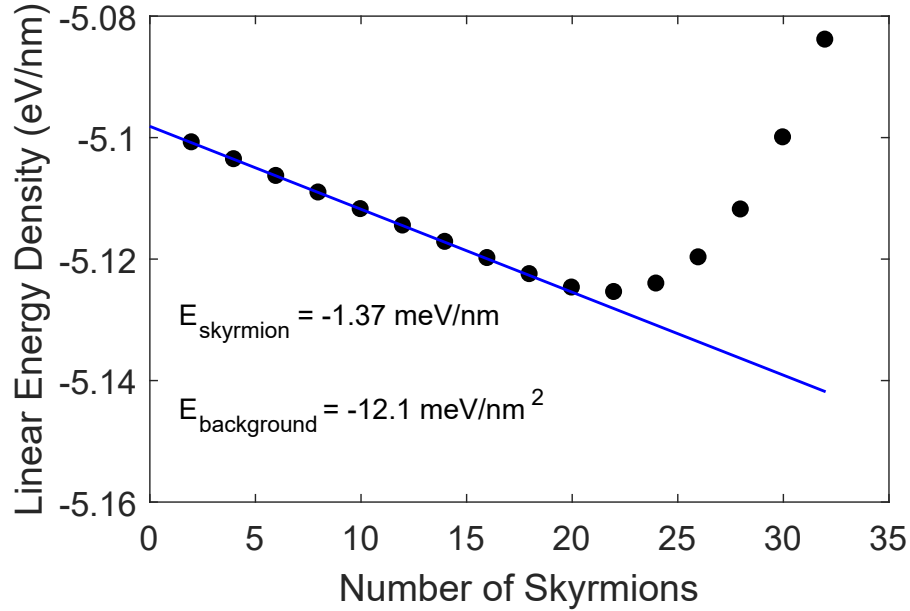the simulation. E_{skyr} will be negative in a regime where skyrmions are energetically favourable. $E_{int}(N)$ is the interaction energy per unit depth between skyrmions and will depend on the inter-skyrmion distance and therefore on N. For small values of N we can assume $E_{int} << E_{skyr}$ and so the energy as a function of N will be linear. Figure 3.6 shows the energy per unit length along the x-direction and is indeed linear at low skyrmionic densities. The fitted line here has a slope that corresponds to the skyrmion self-energy and the intercept corresponds to the background energy for the system. This leads to a background energy of $E_{back} = -12.1$ meV/nm^2. The skyrmion self-energy per unit length was found to be -1.37 meV/nm. Since typical skyrmions have lengths on the order of $\sim 10^1$ nm, typical skyrmion self-energies will be on the order of 10's of meV. The average energy per unit volume is shown in fig. 3.7 with the calculated interaction potential of the skyrmions.
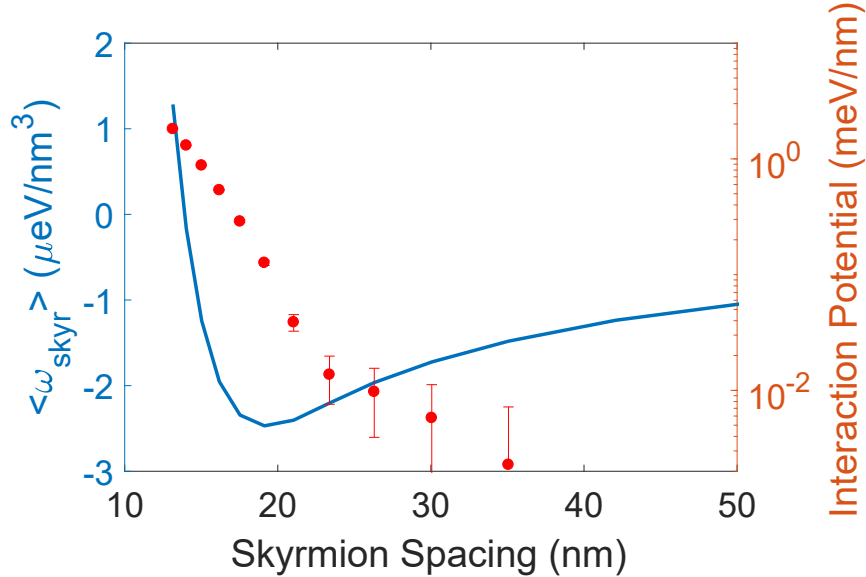
Figure 3.7: The energy density as a function of skyrmion spacing for fields of 500 mT is shown by the blue line. The red dots correspond to the skyrmion-skyrmion interaction potential and is found by subtracting the contribution due to the skyrmion self-energy and the energy of the ferromagnetic background.

By subtracting off the skyrmion self-energy and the background energy and dividing by the number of skyrmion-skyrmion interactions, we can arrive at the interaction potential. Plotting this in terms of inter-skyrmion distance reveals an approximately exponentially decaying potential of the form,

$$V = V_0 e^{-r/\alpha}, \tag{3.5}$$

characteristic of short-range interactions, where α is the exponential constant of approximately 2.3 nm. This is due to the fact that the out-of-plane component of the skyrmion's magnetization is approximately exponentially decaying as a function of radial distance from the skyrmion core. As the inter-skyrmion distance is reduced, the overlap between these tails increases exponentially and so the interaction energy also increases exponentially. Figure 3.8 shows the skyrmion interaction potential plotted alongside the angle of the spins with respect to the field. The interaction potential and the angular decay of the skyrmion have approximately the same exponential constant. The exponential constant, α, is determined to be 2.3 nm.
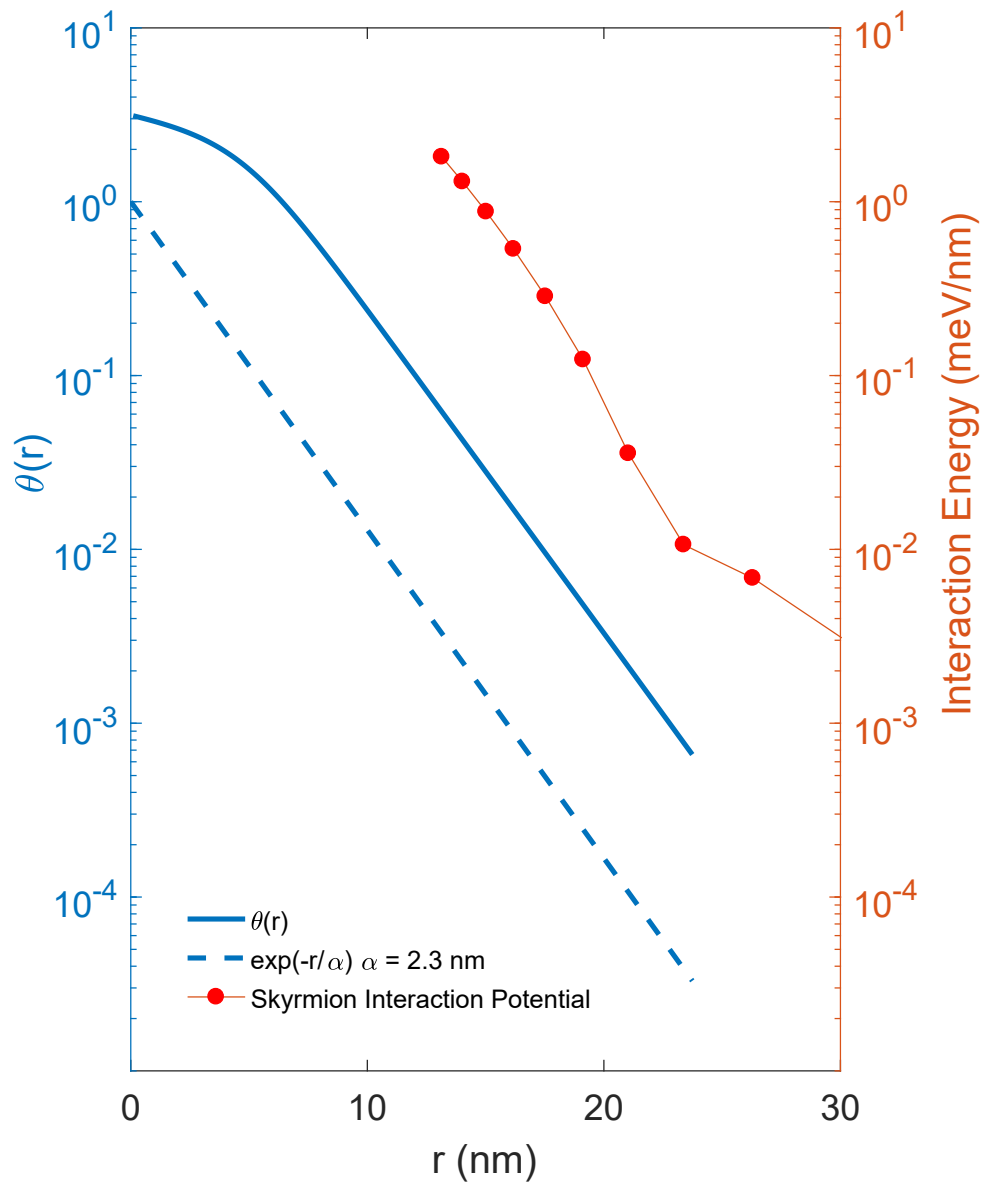
Figure 3.8: The skyrmion-skyrmion interaction potential has a similar functional form to that of the angle with respect to the field direction as a function of distance from the skyrmion core. Both have an exponential constant close to 2.3 nm.

Counter-intuitively, the skyrmion-skyrmion interaction for these systems is strictly repulsive despite the tendency for skyrmions to form well-ordered lattices. The fact that there is a minimum in the energy as a function of skyrmion spacing as shown in fig. 3.7 is sometimes misconstrued as being due to an attractive component in the interaction. This energy minimum corresponds to an optimal skyrmion density rather than a Lennard-Jones-like balance between attractive and repulsive interactions. This minimum is due to the skyrmion self-energy which is often ignored. As the spacing in a skyrmion lattice is increased, the energy increases because more of the system exists in the energetically unfavourable ferromagnetic state. If the spacing between skyrmions becomes too large, the energy can be lowered by adding a skyrmion (which has a negative self-energy) to the system. After accounting for the self-energy, the interaction potential reveals itself to be wholly repulsive. The hexagonal lattice observed in skyrmionic systems is then strictly due to a hexagonal close packing type mechanism [69].

3.4   Elliptically Unstable Skyrmions

Though skyrmions are stable across a range of fields, there will be some point upon lowering the field that the system enters into a region of instability and the magnetic texture transitions into a one-turn helicoidal state. The reason that the skyrmions are unstable below a certain field is referred to as the elliptic instability and the field at which this happens is the strip-out field. This refers to the process by which skyrmions are able to continuously deform into single turn helicoidal structures [41]. A system that is in a skyrmionic phase and has an applied field that is reduced below the point of instability will find that the skyrmions are no longer able to hold their shape.

To understand the process by which these skyrmions elongate, we can look at the energy as a function of strain for two different fields in a micromagnetic simulation. An isolated skyrmion was calculated for a field of $\mu_0 H = 500$ mT and then the spacing between grid points along the y-direction, d_y, was changed from its original value, d_{y0}.

Without relaxing the system, the energy was measured for various spacings. In this way we are probing how the micromagnetic energy responds to small perturbations to the spin configuration. The energy of the background was subtracted by running the same simulation with no skyrmion present. The field is then lowered to $\mu_0 H = 300$ mT. In this field the skyrmion is unstable and will spontaneously elongate if there are no barriers that prevent it from doing so. Because of this instability, for lower fields the equilibrium skyrmion spin configuration for 500 mT was used. Then, without relaxing, d_y was changed in the same way as the 500 mT simulation. The reason why skyrmions become unstable is because as they elongate they acquire a more helicoidal character. So, if the system is in a state where the helicoid is energetically preferable to the skyrmion it will elongate to increase the amount of the system which is in the helicoidal phase.

The energy as a function of $\epsilon = 2(d_y - d_{y0})/(d_y + d_{y0})$ is shown in figure 3.9 for fields of $\mu_0 H = 0.3$ T and at 0.5 T for comparison. At 500 mT the skyrmion displays a Hookian response to small perturbations to the skyrmion shape but at 300 mT this response changes to one whereby the energy of the skyrmion is lowered by increasing the length.

Because there are no energy barriers in the elongation of the skyrmion, they will spontaneously extend in this manner until they encounter an energy barrier. Even though the helicoidal state is the lowest energy phase, the fact that the skyrmion phase is topologically distinct from the helicoidal phase means that there will always be some energy barriers between these phases. Possible energy barriers that could preclude a skyrmionic phase from transitioning to a completely helicoidal phase are the energy barriers preventing a skyrmion-skyrmion fusion and the energy barriers that may exist at grain boundaries due to surface twists.

Initially it was assumed that the system would be in a helicoidal state in accordance with fig. 1.6. However, the spin asymmetry shown in fig. 3.10 is not entirely consistent with the helicoidal texture predicted. The fit obtained for a one-dimensional helicoidal structure is shown by the blue dashed line. The fit is noticeably
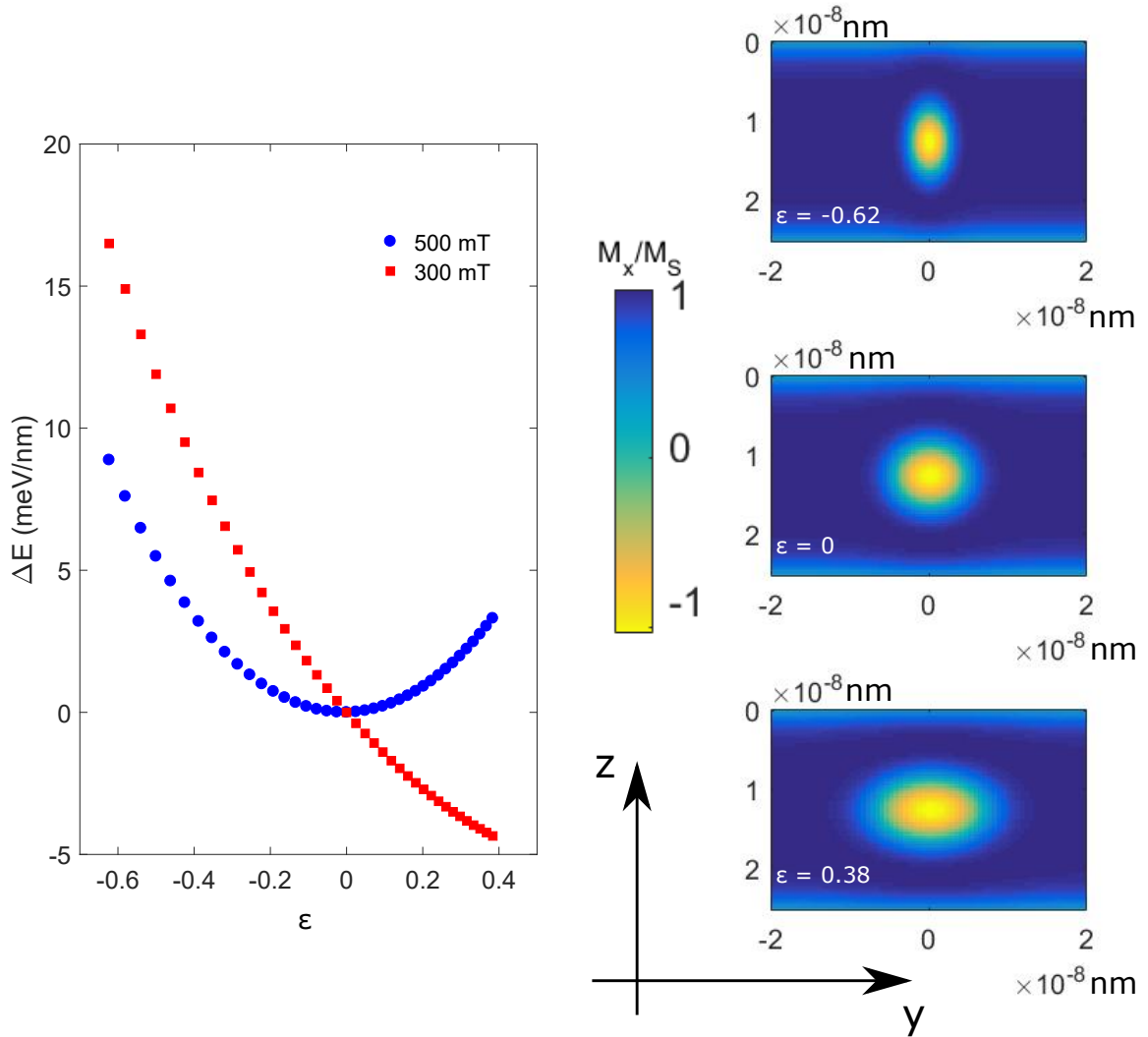
Figure 3.9: The energy of a skyrmion under strain. The blue circles are the energy for a skyrmion at 500 mT. A Hookian response to deformation suppresses the elliptic distortion. At lower values of $\mu_0 H$, below the strip-out field, the energy can be reduced by distorting the skyrmion along the y-direction. This distortion will continue to cause the skyrmion to distort until it encounters an energy barrier like another skyrmion or a grain boundary.
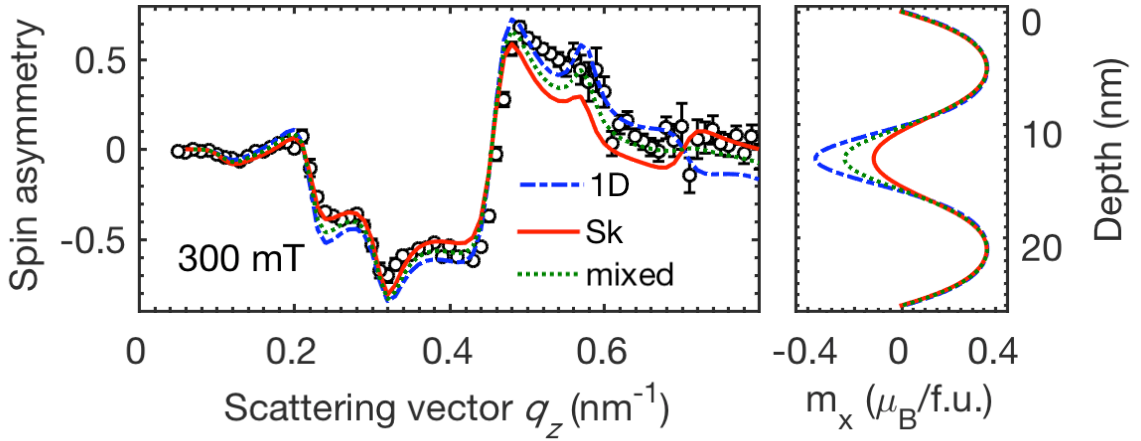
Figure 3.10: The PNR spin asymmetry for $\mu_0 H = 300$ mT. A 1D helicoidal model is insufficient to explain the full PNR data, this is shown by the blue dotted line. The red line shows the fit obtained from a skyrmionic model. This fit noticeably fails to fit the data for $q_z > 0.4$ nm^{-1}. A lattice of elliptically distorted skyrmions was found to be the best fit. The depth profiles are shown to the right of the spin asymmetry.

inconsistent in the high-q_z regime as well between $0.2 < q_z < 0.4$ nm^{-1}. A skyrmionic texture was also compared to the data and is shown is in red. Because skyrmions are unstable at this field, the elliptic instability was suppressed by using an initial state of skyrmions in a chain with a spacing of $L_{Dy} = 22$ nm. Because of the energy barriers preventing skyrmions from coalescing, a skyrmion chain is able to be relaxed even below the elliptic instability. The skyrmionic profile gave a better fit than the the helicoidal profile at low q_z but at $q_z > 0.4$nm^{-1} the fit is inconsistent with the spin asymmetry.

It was found that a mixture between these two phases was a better fit to the spin-asymmetry. We used a periodic array of elliptically distorted skyrmions to obtain the depth profile used. It could be possible that as the field is reduced, the skyrmion array predicted in fig. 3.5 begins to elliptically distort but remains in a metastable state where not all of the skyrmions have coalesced due to energy barriers resulting from the skyrmion-skyrmion interaction potential. An example of half of an elliptically distorted skyrmion is shown in fig. 3.11 b) and is contrasted with a normal skyrmion array shown in a). The left side of this elliptically distorted skyrmion has the texture of a helicoid whereas the right side is similar to a skyrmion. The array of distorted
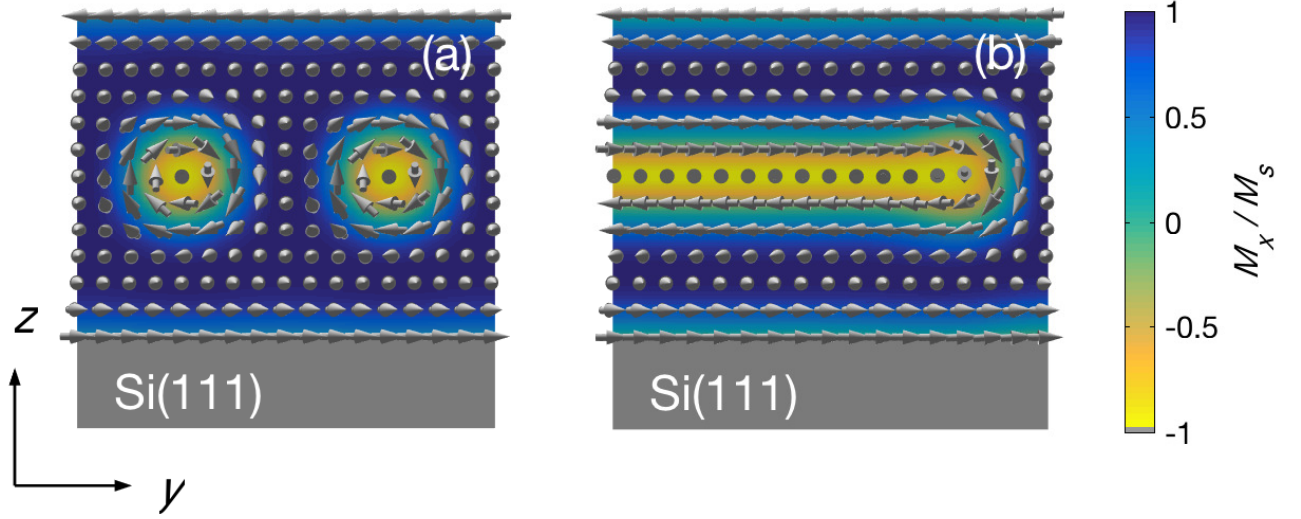
Figure 3.11: The spin configuration for a 1D lattice of in-plane skyrmions and for an elliptically distorted skyrmion. The left side of the elliptically distorted skyrmion is nearly identical to a 1D helicoidal model whereas the right side has a skyrmion-like end cap.

skyrmions is prepared in the micromagnetic calculation by beginning with a single skyrmion in a system of size L_E with periodic boundaries in the x and y-directions. Upon relaxing this system, the skyrmion will elongate until it meets the periodic boundary and encounters itself. The spacing of this elliptically distorted skyrmion array, L_E, is varied which effectively varies the ratio of helicoid segment to skyrmion segment. In the depth profile, this will vary the size of the drop in the moment at the centre of the film.

The spacing of the elongated skyrmion array, L_E, was fit and was found to have a value of 44 ± 17 nm. This corresponds to roughly a system with a half-skyrmion and half-helicoid character. The fit to the spin asymmetry is shown by the green curve in fig. 3.10 and the magnetic depth profile used is shown on the right. The full reflectivity with the fit using a spacing of 44 nm is shown in fig. 3.12 and the inset shows the value of χ^2 for the spin asymmetry as a function of $1/L_E$.

There is another energy barrier at grain surfaces that could provide way to metasta-bilize this elliptically distorted state. Because MnSi films will break up into chiral domains if the underlying substrate is achiral, there will always be grain boundaries
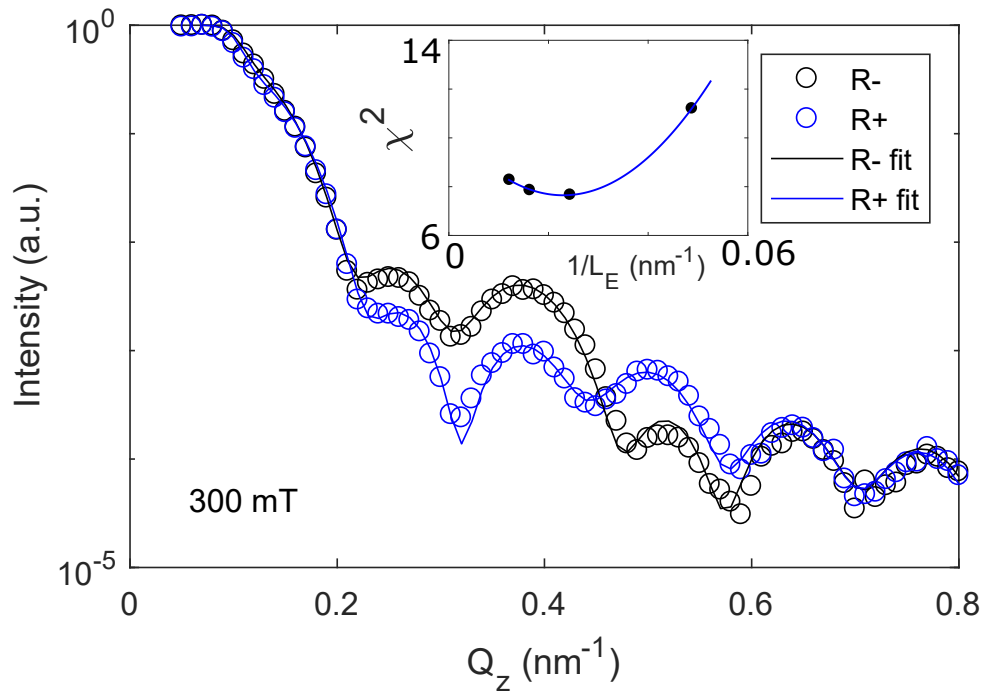
Figure 3.12: The PNR reflectivity for $\mu_0 H = 300$ mT. The inset shows χ^2 as a function of the fit parameter, L_E. The spacing between elliptically distorted skyrmions is minimized for $L_E = 44$ nm.

within the film. If at the grain boundaries the inter-grain exchange coupling is weak compared to the intra-grain interactions it can be shown that the stable state at 300 mT is one with half-skyrmion like end caps. In this model I assume free boundary conditions at the grain edge (the y-direction) and at the film surfaces (z-direction).

With this model I am comparing two different states. One of these is prepared by relaxing a fully helicoidal state and the other is prepared by relaxing a skyrmion. These magnetic states are for a film of thickness 25.2 nm along the z-direction and 102 nm along the y-direction, with periodic boundaries in the x-direction but *not the y-direction*. An in-plane field of 300 mT is applied along the x-direction. The helicoidal state will not greatly change as it is relaxed due to energy barriers at the film edge but the state prepared with a skyrmion will elongate until it reaches the boundaries in the y-direction. These relaxed states are shown in fig. 3.13.

Figure 3.13 a) shows the metastable state that is prepared using the helicoidal model. This is close to what is usually assumed to be the ground state in the helicoidal region of the phase diagram. Figure 3.13 b) shows the energy density for this state. Systems could be caught in this metastable state when increasing $\mu_0 H$ from lower fields where the system exists in a more regular helicoidal magnetic state. This usually assumed helicoid is not the ground state for this system. Figure 3.13 c) shows the lower energy state. This system was prepared using the relaxed skyrmion and features skyrmion-like end-caps. These end-caps are stabilized by the surface twists that result from the free boundary conditions in the y-direction. The energy density is shown in d) and the energy difference between the two systems is 8.95 meV/nm with the elliptical state being of lower energy. Because the grains are 100's of nm in width on average, it must be a combination of both granular end cap barriers and inter-skyrmion barriers that contribute to the magnetic depth profile. This analysis also suggests that by growing wires with granular dimensions that are on the order of the size of skyrmions, it might be possible to utilize the twists due to grain boundaries to stabilize skyrmionic objects well outside the usual realm of stability enabling low-field operation.

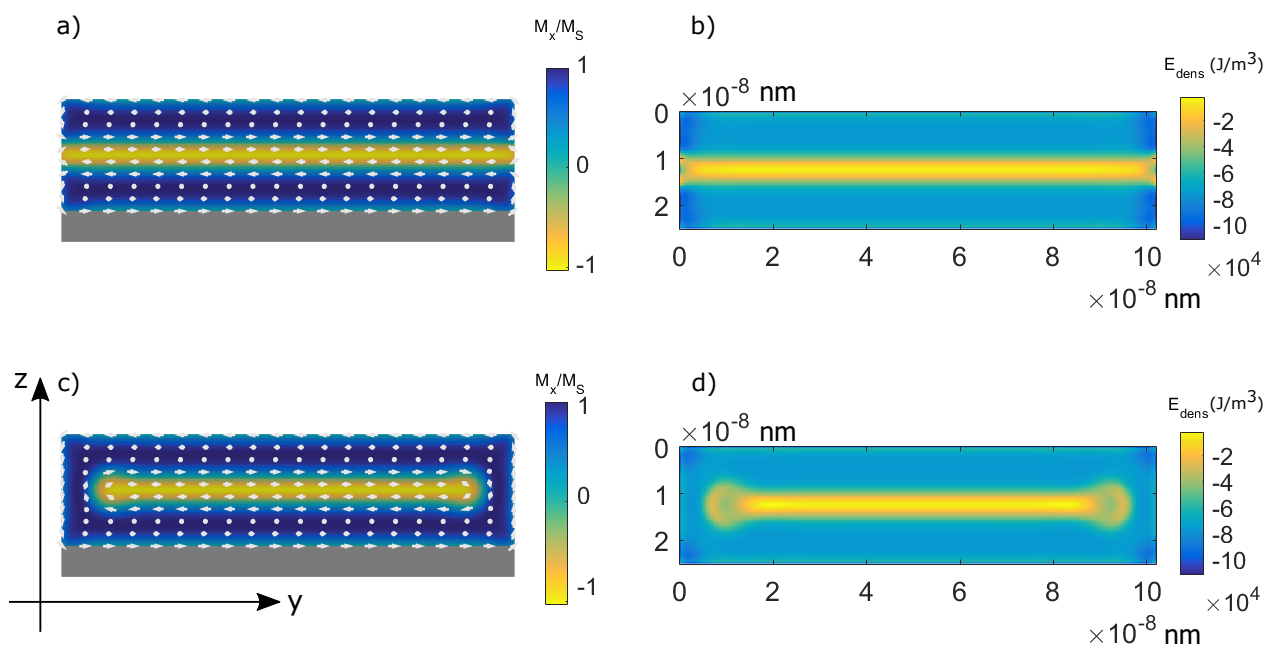Figure 3.13: A comparison between a 1D helicoidal state and an elliptically distorted skyrmion state (the lowest energy state) for fields of 300 mT and free boundaries in the y and z directions. The energy can be reduced in a helicoidal model with free boundaries by introducing skyrmionic end caps near the boundaries in y. These end caps are stabilized by the surface twists that form at the film interfaces.
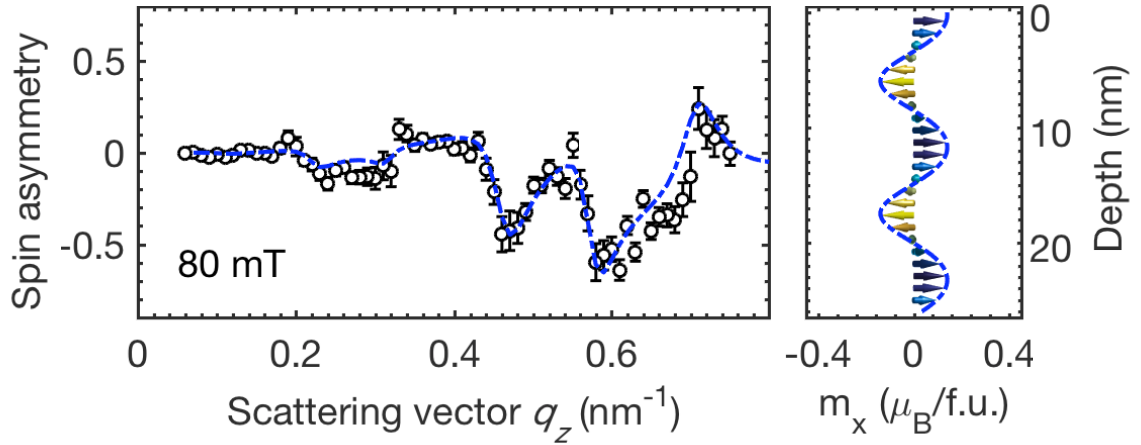
Figure 3.14: The PNR spin asymmetry for fields of $\mu_0 H = 80$ mT. The right side shows the fitted depth profile for this field. The moment for this field is reduced due to the presence of bichiral domains where frustration leads to disorder where helices are rotated with respect to each other. This leads to a cancelling of the moment.

Finally, for the lowest field probed of $\mu_0 H = 80$ mT the system is consistent with the expected helicoidal state. This is shown in fig. 3.14 with the magnetic profile shown to the right of the spin asymmetry. The calculated state is different than what is observed in the spin asymmetry due to the presence of bichiral domains that were shown to exist in ref. [32]. Frustration here creates disorder where the helices are rotated with respect to each other. This leads to cancelling of the magnetization and a reduced total moment.

The PNR measurements presented within this chapter provide the first direct evidence for skyrmions in MnSi thin films and resolve the controversial in-plane phase diagram of MnSi. These skyrmions are noteworthy for being in-plane rather than out-of-plane, which provides interesting opportunities to explore geometries that might not otherwise be possible for OOP skyrmions. In order to make progress in the emerging field of skyrmionics, it is necessary to understand the conditions under which skyrmions might be able to nucleate and in particular, the role that uniaxial anisotropy plays in skyrmion stability.

Chapter 4

MnSi/SiC(0001)

Our previous work in MnSi/Si found a hard axis magnetocrystalline anisotropy induced by the tensile epitaxial mismatch between the MnSi film and the Si(111) substrate. This hard axis anisotropy precludes the existence of out-of-plane (OOP) skyrmions. A natural next step is then to ask whether or not it is possible to reverse this anisotropy by changing the sign of the epitaxial mismatch. The SiC(0001) surface unit cell is 4.6% smaller than the surface unit cell for MnSi(111) and so this section aims to explore the growth of MnSi(111) on SiC(0001) substrates.I will cover the crystal structure and properties of these thin films with particular emphasis on the atomic force microscopy and Hall-bar electrical measurements.

We find that though we were able to achieve growth of B20 MnSi(111)/SiC(0001), the growth mode is substantially more complicated than that of MnSi/Si. In particular, the high temperatures needed for this growth lead to a dewetting that arises from film edge capillary instabilities. This relieves the strain in the crystal leading to a nearly unstrained MnSi film that acquires a small amount of tensile strain due to a difference in thermal expansion coefficients.

Further complicating the analysis is the fact that while the majority of the film exists in the desired orientation of the MnSi crystal with respect to substrate, the film is polycrystalline in nature resulting in an ensemble of orientations. The electrical properties support the hypothesis that the film is in a nearly unstrained state with some small amount of residual tensile strain and a hard-axis anisotropy.

4.1 Crystal Structure

Reflection high-energy electron diffraction (RHEED) demonstrates that the film is composed of an ensemble of B20 MnSi grains. These *in-situ* electron diffraction
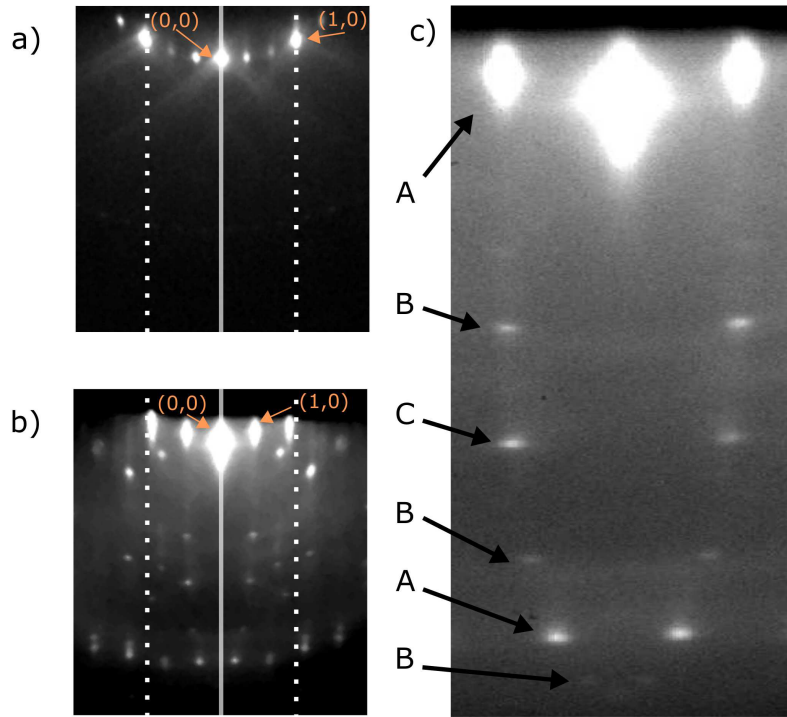
Figure 4.1: Reflection high energy electron diffraction patterns for *in-situ* MnSi/SiC. The pattern for the underlying SiC substrate is shown in a) along the same direction as shown in b). The (1,0) spots in SiC have twice the spacing of the (1,0) spots for the MnSi lattice in k-space. Rotation of the grains with respect to the underlying substrate leads to multiple reflections. These reflections have been labelled as A, B and C which correspond to the 0°, 16.1° and 30° respectively.

studies are shown in fig. 4.1. Figure 4.1 a) shows the RHEED pattern for the SiC substrate and fig. 4.1 b) shows the RHEED pattern for a 15 nm MnSi film grown on top, both images are taken along the same direction. The (1,0) reflections for both images are consistent with the desired orientation of the film with respect to the substrate, $[1\bar{1}0]$MnSi(111)$\|$$[1\bar{1}00]$SiC(0001). The bright, sharp spots indicate a smooth MnSi surface. Figure 4.1 c) shows b) in more detail. In fig. 4.1 c), an elliptical ring appears in the diffraction pattern. In addition to the (1,0) and (-1,0) diffraction spots, a number of other diffraction spots appear. The extra spots along this curve are due to extra domains that have MnSi(111)$\|$SiC(0001) but with their IP crystallographic directions rotated with respect to each other by some angle, ϕ. The letters correspond to unique orientations with respect to the substrate.

An Ewald sphere construction was used to determine the offset angle of these additional orientations. The A-orientation has $[1\bar{1}0]$MnSi(111)$\|[11\bar{2}0]$SiC(0001) and is defined as $\phi = 0$. The B-orientation has $\phi = 16.1°$ and the C-orientation has $\phi = 30°$. Though the faint ellipse indicates that there are very many orientations present, the bright spots indicate that there are 3 clearly dominant orientations and the A-orientation is the most common. These angles are consistent with our prediction using a near-coincidence site-lattice (NCSL) model.

Both X-ray diffraction and transmission electron microscopy (TEM) were used to determine the IP and OOP lattice constants relative to that of bulk MnSi. Both found evidence indicative of a small but tensile strain, opposite of the expected compressive strain that would arise due to the mismatch between lattice constants.

Atomic force microscopy (AFM) measurements were performed on the MnSi samples grown on SiC substrates. Measurements were performed *ex-situ* using an ATEC-CONT tip with a force constant of 0.2 N/m in contact mode. Atomic force microscopy measurements were used to help determine the physical mechanisms responsible for relieving the strain from the epitaxial mismatch.

A TEM dark field image for the $\phi = 0°$ orientation and a 3 QL sample is shown in fig. 4.2 a). It is possible to image only one particular orientation by positioning the aperture such that it only admits light from a diffraction corresponding to the grain of interest. The inter-grain coherence length appears to be larger than the grains themselves suggesting that they share a common origin. Although RHEED indicates that there are multiple orientations of MnSi present, TEM shows that the islands have a coherent orientation within not only single island but also cohere over a length larger than a single island. Figure 4.2 b) shows a 0° dark field image for a thicker 15 nm sample. In this case the coherence is much larger than the grains shown in a), suggesting that as material is deposited the grains coalesce into a single, much larger grain.

Figure 4.2: Dark field TEM images of MnSi(111)/SiC(0001) films. A 3QL template is shown in a) and a 15 nm sample shown in b).

Though strain can lead to energetics that can drive dewetting, the similarity between these films and those of Au films on silica substrates suggests that it is a mechanism primarily driven by surface energy effects rather than interfacial strain[31][65].

Although it is likely that the substrate is initially covered by the amorphous 3 QL template layer, the film has undergone a fingering instability dewetting process at some point during annealing. This dewetting leads to the serpentine islands shown in fig. 4.4 a). These islands have an average width of approximately 100 nm and a length of approximately 350 nm as determined with AFM.

These serpentine islands are due to a fingering instability in the films. A fluctuation in the film that penetrates to the substrate can grow in size and will create the serpentine voids that we can see in fig. 4.4 a). After this hole forms, a small instability on the hole edge will retract according to

$$x_0 \propto t^n, \tag{4.1}$$

where x_0 is the radius of the hole and t is time. We will have $n \sim 0.4$ to 0.5 for holes in single crystal films [65].

The holes in the film are probably forming due to the hillock formation instability which is a compressive strain relief mechanism that occurs during heating [65]. After

this instability reaches the substrate it will begin to retreat. Mass will begin to diffuse over the edge in order to reduce the curvature. As the mass diffuses, the bottom of the hole will begin to retreat. This is shown in fig. 4.3 a). The curvature at the edge of the film is always greater than that of the film surrounding the hole and therefore material will continue to diffuse [65].

The reason for the finger stability is that material builds up on the film edge as the film edge retreats. Where the film is thinner, the film will retract more quickly. Because as the thinner film retreats it cuts into the middle of the film where there is less material creating an unstable retreat mechanism. This causes this instability to retreat even more quickly and the finger-like void will continue to grow. This is shown in fig. 4.3 b) and c). Eventually the fingers are pinched off due to a valley that continues to develop as the film retreats. This valley develops as a consequence of curvature minimization after a build up of material along film edges as well as a consequence of the Plateau-Rayleigh instability. Eventually the valley becomes deep enough to reach the substrate and a new edge is formed and the process may repeat [65].

TEM measurements determine that the smaller crystallites shown in the yellow circle in fig. 4.4 are polycrystalline MnSi. These polycrystalline features are found in all of the MnSi/SiC samples and are the likely reason behind the faint ellipse-like curve shown in fig. 4.1 c).

Figure 4.4 b) shows a 3 QL template with 15 nm of material deposited on top. As material arrives on the template, the islands grow. Though the film is discontinuous initially, eventually it will form a contiguous network of grains. This dewetting is likely allowing for strain relief at the substrate-film interface, as evidenced by the near zero and tensile strain observed by X-ray and TEM. Upon cooling the film after the growth the tensile strain can be understood with the observation that the thermal expansion coefficients for MnSi and SiC differ. For MnSi the thermal expansion coefficient is $\alpha_{\text{MnSi}} = 1.2 \times 10^{-5}$ K^{-1} [64] and SiC is $\alpha_{\text{SiC}} = 3.3 \times 10^{-6}$ K^{-1} [43]. Since as the film is cooled, the substrate will shrink slower than the MnSi, the mismatch will grow like

Figure 4.3: Amorphous MnSi films will undergo a fingering instability upon annealing. Material will diffuse from regions of high curvature to regions of low curvature. This results in receding of edges and the diffusion of material away from thinner regions, which is shown in a) and b). The fingering instability is a result of the fact that thinner regions diffuse faster than thicker regions. As a thin instability retreats the hole cuts into progressively thinner regions in the middle of the film which results in an even faster retreat. This is shown in c).

Figure 4.4: Atomic force microscopy images for MnSi/SiC substrates. A 3 QL template is shown in a). The serpentine domains are the result of a fingering instability that occurs as the material is heated. b) shows a thicker film of 15 nm. As material is codeposited on to the thinner films, the islands coalesce into larger grains. A larger, 6 QL, template is shown in c). AFM has caught the film in the process of dewetting as evidenced by the fact that some serpentine islands can still be seen. The smaller serpentine grains are still present. The larger grains have triangular holes in them. Because the triangular holes form edges along the $[1\bar{1}0]$ direction in MnSi, we can determine the orientation of the film with respect to the substrate. d) shows a crystallographic analysis of the film shown in c) where the grains are organized by orientation. A corresponds to the 0° orientation, B corresponds to the 16.1° orientation and C corresponds to the 30° orientation. The primed grains have the same epitaxial relationship to the substrate as the unprimed grains but have different orientations relative to their unprimed counterparts [46].

$T\Delta\alpha = T(\alpha_{MnSi} - \alpha_{SiC})$. For growth temperatures of 500°C there could be as much as 0.4% tensile strain developing during cooling.

Figure 4.4 c) shows a 6 QL template grown with solid phase epitaxy (SPE). SPE is a growth method where a metastable amorphous layer crystallizes on a single-crystal substrate, usually through annealing. A thicker film decreases the speed at which the film dewets, as evidenced by the larger islands. The dewetting in this case primarily occurs within the large grains, shown by the large triangular holes. Though there are grains here with these large holes, the fingering instability can still be seen in the 6 QL template as highlighted by the red circle. Because of the thicker template, the film has been caught in a state of dewetting.

We can exploit the fact that MnSi naturally forms edges along the $\langle 1\bar{1}0 \rangle$ direction to perform crystallography with AFM [22]. Figure 4.4 d) shows a 6 QL film where grains are highlighted by their angle with respect to $[1\bar{1}00]$SiC. The grains are marked by A, B and C which correspond to the 0°, 16.1° and 30° respectively. The primed orientations mark grains that are rotated 60° with respect to their unprimed counterparts. The primed grains will have the same epitaxial relationship to the underlying substrate as the unprimed counterparts but will have different orientations with respect to each other. The need for primed and unprimed grains is because of the fact that MnSi has a threefold axis of symmetry and SiC has a sixfold axis of symmetry running parallel about the film normal.

By measuring the area of the grains and their respective orientations over an ensemble of three films, we find that the coverage of the 0°, 16.1° and 30° orientations are roughly $51 \pm 10\%$, $25 \pm 8\%$ and $24 \pm 4\%$ respectively. This is consistent with what was observed in TEM and RHEED. An analysis of one of these AFM images is shown in fig. 4.4 d). This statistical analysis is consistent with the results found in TEM and RHEED which suggested that the 0° orientation is the most common but that the 16.1° and 30° orientation are present in moderate amounts.

Films such as the one shown in fig. 4.4 b) were found to be electrically continuous whereas thinner films such as those shown in a) and c) were found to be insulating.

This is due to the contiguity of grains, which we can see is achieved in the case of the film with 15 nm of material, but is not achieved for thinner samples.

4.2 Electrical Properties

Because the electrical measurements have contributions that depend on M, abrupt phase transitions can be measured and it can be determined whether or not the magnetic phase diagram is consistent with the observed strain. Because only the thicker samples were found to be electrically conductive, electrical measurements were only performed on a 15 nm sample similar to that shown in fig. 4.4 b). A sample with a 3 QL thick template and 15 nm of codeposited MnSi capped with a 20 nm amorphous Si cap was used with a Quantum Design Physical Properties Measurement System (PPMS) to probe the electrical properties of MnSi/SiC using a standard hall bar geometry as detailed in chapter 2. Because our previous measurements of MnSi/Si showed that a tensile strain resulted in a hard-axis magnetocrystalline anisotropy, we anticipated that these MnSi/SiC films would demonstrate similar magnetic properties. The electrical measurements show behaviour similar to that of MnSi/Si(111). This is consistent with the observed strain, which was found with TEM and XRD to be tensile as opposed to compressive. A tensile strain implies a hard-axis magnetocrystalline anisotropy and so we would expect similar magnetic behaviour.

Figure 4.5 shows the resistivity as a function of temperature for a 15 nm thick film grown on a SiC substrate and its derivative with respect to T. The derivative of this can indicate phase changes. The peaks in $d\rho/dT$ at 39.6$\pm$0.5 K indicates a Curie temperature $T_C = 39.6$ K similar to that of MnSi/Si(111) ($T_C = 42$K). The increase in Curie temperature from the bulk value of $T_C = 29.5$ K is due to the increased unit cell volume [32].

The resistivity, ρ_{xx}, is about 1.5 times higher than that of the MnSi/Si(111) films. We report a resistivity, $\rho_{xx} = 2.78 \times 10^{-6}$ Ωm. The residual resistivity ratio,

$$\text{RRR} = \frac{\rho_{xx}(T = 300 \text{ K})}{\rho_{xx}(T = 0 \text{ K})} = 21.6, \tag{4.2}$$

Figure 4.5: Longitudinal resistivity as a function of temperature for a 15 nm film. The derivative of this is a way of determining the Curie temperature which was found to be 39.6±0.5 K.

is comparable to MnSi. This indicates that the elevated resistivity is not due to defects in the film but rather could be due to a smaller effective thickness of the film. The growth is such that the template is discontinuous and during the codeposition process islands grow until they eventually connect into a continuous film. This interpretation is further supported by the AFM results above and the fact that samples below a thickness of 15 nm were found to insulating.

Figure 4.6 a) shows the magnetoresistance of MnSi/SiC(0001), which is defined as

$$\text{MR} = \frac{\rho_{xx} - \rho_0}{\rho_0}, \tag{4.3}$$
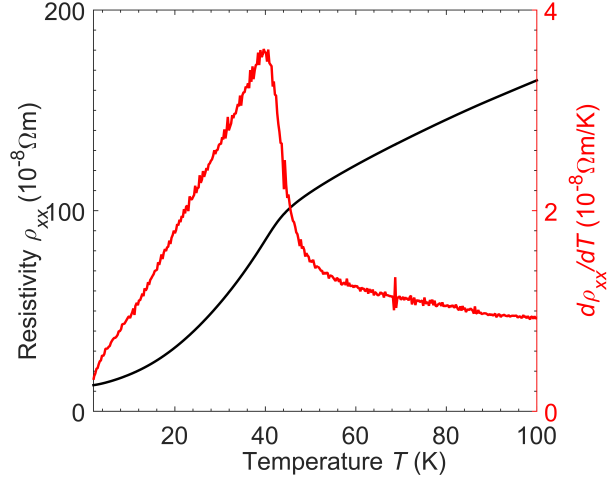
where ρ_0 is the resistivity at zero field. The inset shows the derivative of the magnetoresistance with respect to the applied field. The peak in this provides a way of estimating the transition field between the conical and ferromagnetic states in MnSi/Si. We estimate this field to be $\mu_0 H_{C2} = 0.93 \pm 0.05$ T. These measurements are consistent with a hard axis magnetocrystalline anisotropy and are very similar to those of MnSi/Si. The magnetoresistance for a 25.4 nm film of MnSi/Si(111) is shown in fig. 4.7 a). This field is larger than the intrinsic bulk value, H_D, primarily due to the demagnetizing field which will produce an effective field opposite to the

applied field.

The Hall resistivity, ρ_{xy}, also demonstrates that the magnetic properties are consistent with what would be expected from the observed strain. Measuring the Hall resistivity can provide a means to probe topological magnetic changes as described in chapter 2. The Hall resistivity is shown in fig. 4.6 b). The behaviour shows no sign of a first order phase transition that would be expected for a skyrmionic state. Figure 4.7 b) shows Hall resistivity for a MnSi/Si(111) sample of thickness 25.4 nm. The Hall resistivity of this sample is similar to that of the MnSi/SiC(0001) which is consistent with a hard axis magnetocrystalline anisotropy and the observed strain.

Though the mismatch would imply a compressive strain and an easy axis anisotropy, dewetting mechanisms prevent epitaxial compressive strain from forming. The electrical measurements are consistent with the interpretation that the small tensile strain that develops during cooling produces an easy-plane anisotropy similar to that which is present in MnSi/Si epitaxial films.

Though the easy-axis anisotropy predicted was unable to be achieved through the growth of MnSi on SiC substrates because of dewetting mechanisms, interesting geometric structures were formed as a result of these dewetting mechanisms. The geometries provided by these films could be an interesting system to explore in the future and the surface edge states provided by the serpentine wires might provide a means to stabilize OOP skyrmions.
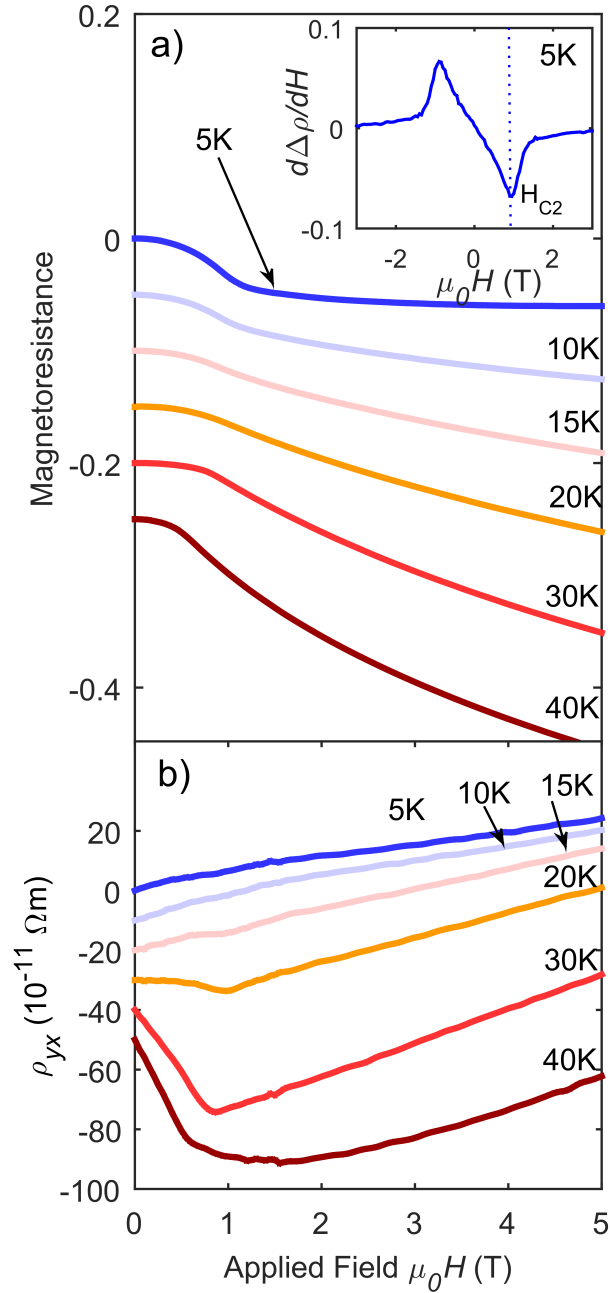
Figure 4.6: Magnetoresistance, a) and the Hall resistivity, b) as a function of applied field for a 15 nm MnSi/SiC film. A peak in the derivative of the magnetoresistance provides a way of determining, $\mu_0 H_{C2}$, the critical field when the film transitions from a conical state to saturated ferromagnetic state.
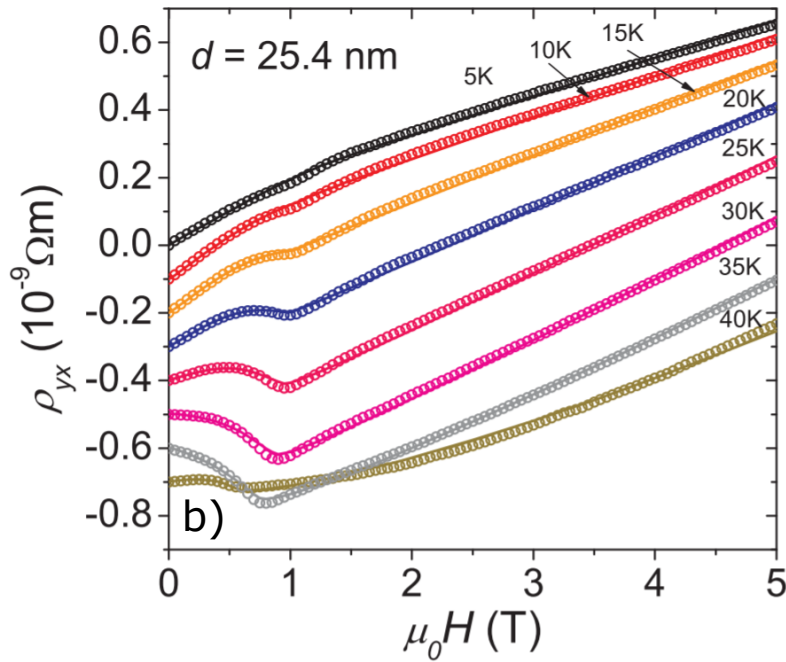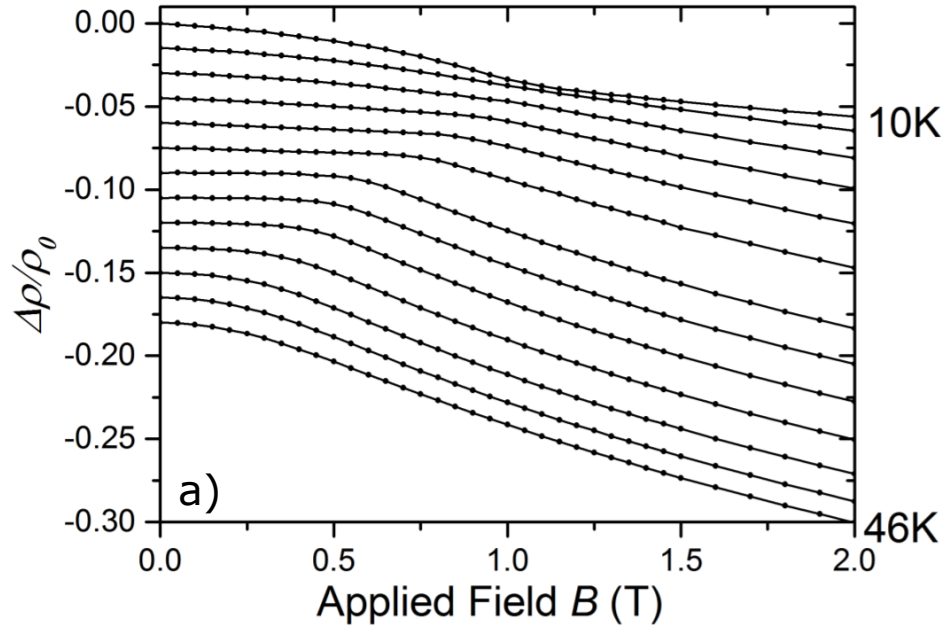
Figure 4.7: Magnetoresistance [75] and Hall resistivity [49] of MnSi/Si thin films. The behaviour looks qualitatively similar to MnSi/SiC, indicating the magnetic state is the same as MnSi/Si.

Chapter 5

Conclusions

The phase diagram for in-plane fields in epitaxial MnSi/Si thin films was resolved using polarized neutron reflectometry. This technique is sensitive to the magnetic depth profile of these films and so can be used to resolve magnetic variation along the film normal. A phase of in-plane skyrmions was uncovered at $T = 25$ K and $\mu_0 H = 0.5$ T. These skyrmions have their axis of symmetry pointing within the plane of the film in contrast to the more common out-of-plane skyrmions. Skyrmions spontaneously order into a 1-dimensional lattice that was found to have a spacing of 21 nm.

At higher fields (700 mT) it was demonstrated that the films are in a twisted ferromagnetic state where the magnetization varies little throughout the centre of the film but near the edges there are magnetic twists.

At lower fields (300 mT) it was discovered that these in-plane skyrmions will elongate through a process called the elliptic instability. It was found that energy barriers prevent these skyrmions from fully coalescing into the stable helicoidal state. The model used was a 1-dimensional lattice of elliptically elongated skyrmions which were found to be 44 nm on average. A combination of barriers resulting from grain boundaries and the barriers that exist for merging skyrmionic end caps may be resulting in the film existing in this metastable state.

A method for changing the sign of the uniaxial anisotropy was explored that exploits the mismatch between MnSi(111) and SiC(0001). Because this mismatch has the opposite sign of MnSi on Si it was thought that the anisotropy would change sign. Because of surface energetics, the film undergoes a fingering instability as the film is heated. Additionally, a variety of domains each with a different epitaxial relationship relative to the substrate were found to have nucleated. As the film

is cooled, a very small tensile strain develops, which leads to a magnetic anisotropy similar to MnSi/Si. This tensile strain is a result of the difference in thermal expansion coefficients. The magnetic behaviour was found to be very similar to MnSi/Si as would be expected from the anisotropy. The magnetic structure was probed using electrical measurements and the morphological structure was probed using atomic force microscopy and transmission electron microscopy.

The role of uniaxial anisotropy and the effect of confinement in epitaxial chiral films is explored through two different methods in this thesis. It was found that in-plane skyrmions are stabilized in MnSi/Si films. Though a change in the sign of the anisotropy was not found, morphologically interesting structures were able to be produced. It is possible that these structures could produce interesting geometries to explore in the future.

Bibliography

[1] M. N. Baibich, J. M. Broto, A. Fert, F. Nguyen Van Dau, F. Petroff, P. Eitenne, G. Creuzet, A. Friederich, and J. Chazelas. Giant magnetoresistance of (001)Fe/(001)Cr magnetic superlattices. *Physical Review Letters*, 61(21):2472–2475, 1988.

[2] P Bak and M H Jensen. Theory of helical magnetic structures and phase transitions in MnSi and FeGe. *Journal of Physics C: Solid State Physics*, 13(31):L881–L885, 1980.

[3] J Barzilai and J M Borwein. 2-Point Step Size Gradient Methods. *Ima J Numer Anal.*, 8(1):141–148, 1988.

[4] L. Berger. Side-jump mechanism for the hall effect of ferromagnets. *Physical Review B*, 2(11):4559–4566, 1970.

[5] L. Berger. Low-field magnetoresistance and domain drag in ferromagnets. *Journal of Applied Physics*, 49(3):2156–2161, 1978.

[6] L Berger. Emission of spin waves by a magnetic multilayer traversed by a current. *Phys Rev B*, 54(13):9353–9358, 1996.

[7] M V Berry. Quantal Phase Factors Accompanying Adiabatic Changes. *Proceedings of the Royal Society of London A: Mathematical, Physical and Engineering Sciences*, 392(1802):45–57, 1984.

[8] G. Binasch, P. Grünberg, F. Saurenbach, and W. Zinn. Enhanced magnetoresistance in layered magnetic structures with antiferromagnetic interlayer exchange. *Physical Review B*, 39(7):4828–4830, 1989.

[9] B. Binz and A. Vishwanath. Chirality induced anomalous-Hall effect in helical spin crystals. *Physica B: Condensed Matter*, 403(5-9):1336–1340, 2008.

[10] S. J. Blundell. *Oxford master series in condensed matter physics*. Oxford University Press, Oxford, 2001.

[11] A. Bogdanov, U. Rößler, and A. Shestakov. Skyrmions in nematic liquid crystals. *Physical Review E*, 67(1):1–8, 2003.

[12] A.N. Bogdanov and D.A. Yablonskii. Thermodynamically stable "vortices" in magnetically ordered crystals. The mixed state of magnets. *Zh. Eksp. Teor. Fiz*, 95(1):178, 1989.

[13] A. B. Butenko, A. A. Leonov, U. K. Rößler, and A. N. Bogdanov. Stabilization of skyrmion textures by uniaxial distortions in noncentrosymmetric cubic helimagnets. *Physical Review B - Condensed Matter and Materials Physics*, 82(5):1–4, 2010.

[14] A. Chacon, A. Bauer, T. Adams, F. Rucker, G. Brandl, R. Georgii, M. Garst, and C. Pfleiderer. Uniaxial Pressure Dependence of Magnetic Order in MnSi. *Physical Review Letters*, 115(26):1–6, 2015.

[15] B. Dieny, V. S. Speriosu, S. S P Parkin, B. A. Gurney, D. R. Wilhoit, and D. Mauri. Giant magnetoresistive in soft ferromagnetic multilayers. *Physical Review B*, 43(1):1297–1300, 1991.

[16] I. E. Dzyaloshinskii. Theory of Helicoidal Structures in Antiferromagnets. *Soviet Physics-JETP*, 20(3):665–671, 1965.

[17] Lukas Exl, Simon Bance, Franz Reichel, Thomas Schrefl, Hans Peter Stimming, and Norbert J. Mauser. LaBonte's method revisited: An effective steepest descent method for micromagnetic energy minimization. *Journal of Applied Physics*, 115(17):128–131, 2014.

[18] A. Fert, V. Cros, and J. Sampaio. Skyrmions on the track. *Nature Nanotechnology*, 8(3):152–156, 2013.

[19] P. P. Freitas and L. Berger. Observation of s-d exchange force between domain walls and electric current in very thin Permalloy films. *Journal of Applied Physics*, 57(4):1266–1269, 1985.

[20] Helmut Fritzsche. Polarized Neutron Reflectometry As a Unique Tool in Magnetization Reversal. pages 265–271, 2006.

[21] L. Gan, S. H. Chung, K. H. Aschenbach, M. Dreyer, and R. D. Gomez. Pulsed-current-induced domain wall propagation in Permalloy patterns observed using magnetic force microscope. *IEEE Transactions on Magnetics*, 36(5 I):3047–3049, 2000.

[22] B. Geisler, P. Kratzer, T. Suzuki, T. Lutz, G. Costantini, and K. Kern. Growth mode and atomic structure of MnSi thin films on Si(111). *Physical Review B - Condensed Matter and Materials Physics*, 86(11):1–7, 2012.

[23] S. V. Grigoriev, S. V. Maleyev, A. I. Okorokov, Yu O. Chetverikov, P. Böni, R. Georgii, D. Lamago, H. Eckerlebe, and K. Pranzas. Magnetic structure of MnSi under an applied field probed by polarized small-angle neutron scattering. *Physical Review B - Condensed Matter and Materials Physics*, 74(21):1–10, 2006.

[24] Christian Hanneken, Fabian Otte, André Kubetzka, Bertrand Dupé, Niklas Romming, Kirsten Von Bergmann, Roland Wiesendanger, and Stefan Heinze. Electrical detection of magnetic skyrmions by non-collinear magnetoresistance. *Nature Nanotechnology*, 10(12):1039–1043, 2015.

[25] Masamitsu Hayashi, Luc Thomas, Rai Moriya, Charles Rettner, and Stuart S P Parkin. Current-Controlled Magnetic Domain-Wall Nanowire Shift Register. *Scientific Reports*, 320(April):209–211, 2008.

[26] Shougo Higashi, Pavel Kocán, and Hiroshi Tochihara. Reactive epitaxial growth of MnSi ultrathin films on Si(111) by Mn deposition. *Physical Review B - Condensed Matter and Materials Physics*, 79(20):1–7, 2009.

[27] Mahbube Hortamani, Peter Kratzer, and Matthias Scheffler. Density-functional study of Mn monosilicide on the Si(111) surface: Film formation versus island nucleation. *Physical Review B - Condensed Matter and Materials Physics*, 76(23):1–9, 2007.

[28] D. M. Hwang, T. S. Ravi, R. Ramesh, Siu Wai Chan, C. Y. Chen, L. Nazar, X. D. Wu, A. Inam, and T. Venkatesan. Application of a near coincidence site lattice theory to the orientations of YBa2Cu3O7-x grains on (001) MgO substrates. *Applied Physics Letters*, 57(16):1690–1692, 1990.

[29] S. Ikeda, J. Hayakawa, Y. Ashizawa, Y. M. Lee, K. Miura, H. Hasegawa, M. Tsunoda, F. Matsukura, and H. Ohno. Tunnel magnetoresistance of 604% at 300 K by suppression of Ta diffusion in CoFeBMgOCoFeB pseudo-spin-valves annealed at high temperature. *Applied Physics Letters*, 93(8):2006–2009, 2008.

[30] T. Jeong and W. E. Pickett. Implications of the B20 crystal structure for the magnetoelectronic structure of MnSi. *Physical Review B - Condensed Matter and Materials Physics*, 70(7):1–8, 2004.

[31] E. Jiran and C. V. Thompson. Capillary instabilities in thin films. *Journal of Electronic Materials*, 19(11):1153–1160, 1990.

[32] E Karhu, S Kahwaji, T L Monchesky, C Parsons, M D Robertson, and C Maunders. Structure and magnetic properties of MnSi epitaxial thin films. *Phys Rev B*, 82(18):184417, 2010.

[33] E. A. Karhu, S. Kahwaji, M. D. Robertson, H. Fritzsche, B. J. Kirby, C. F. Majkrzak, and T. L. Monchesky. Helical magnetic order in MnSi thin films. *Physical Review B - Condensed Matter and Materials Physics*, 84(6):3–6, 2011.

[34] E. A. Karhu, U. K. Rößler, A. N. Bogdanov, S. Kahwaji, B. J. Kirby, H. Fritzsche, M. D. Robertson, C. F. Majkrzak, and T. L. Monchesky. Chiral modulations and reorientation effects in MnSi thin films. *Physical Review B - Condensed Matter and Materials Physics*, 85(9):1–12, 2012.

[35] Eric A Karhu. *Structural and Magnetic Properties of Epitaxial MnSi(111) Thin Films.* PhD thesis, Dalhousie University, 2012.

[36] Robert Karplus and J. M. Luttinger. Hall effect in ferromagnetics. *Physical Review*, 95(5):1154–1160, 1954.

[37] A V Khvalkovskiy, D Apalkov, S Watts, R Chepulskii, R S Beach, A Ong, X Tang, A Driskill-Smith, W H Butler, P B Visscher, D Lottis, E Chen, V Nikitin, and M Krounbi. Basic principles of STT-MRAM cell operation in memory arrays. *J. Phys. D*, 074001(46 - 074001):1–20, 2013.

[38] N. S. Kiselev, a. N. Bogdanov, R. Schäfer, and U K Rößler. Chiral skyrmions in thin magnetic films: new objects for magnetic storage technologies? *Journal of Physics D: Applied Physics*, 44(39):392001, 2011.

[39] M. Kläui, H. Ehrke, U. Rüdiger, T. Kasama, R. E. Dunin-Borkowski, D. Backes, L. J. Heyderman, C. A F Vaz, J. A C Bland, G. Faini, E. Cambril, and W. Wernsdorfer. Direct observation of domain-wall pinning at nanoscale constrictions. *Applied Physics Letters*, 87(10):2003–2006, 2005.

[40] A. O. Leonov, I. E. Dragunov, U. K. Rößler, and A. N. Bogdanov. Theory of skyrmion states in liquid crystals. *Physical Review E - Statistical, Nonlinear, and Soft Matter Physics*, 90(4):3–8, 2014.

[41] A. O. Leonov, T. L. Monchesky, N. Romming, A. Kubetzka, A. N. Bogdanov, and R. Wiesendanger. The properties of isolated chiral skyrmions in thin magnetic films. *New Journal of Physics*, 18(6), 2016.

[42] Yufan Li, N. Kanazawa, X. Z. Yu, A. Tsukazaki, M. Kawasaki, M. Ichikawa, X. F. Jin, F. Kagawa, and Y. Tokura. Robust formation of skyrmions and topological hall effect anomaly in epitaxial thin films of MnSi. *Physical Review Letters*, 110(11):1–5, 2013.

[43] Z. LI and R. C. BRADT. Thermal Expansion and Thermal Expansion Anisotropy of SiC Polytypes. *Journal of the American Ceramic Society*, 70(7):445–448, 1987.

[44] Zi An Li, Fengshan Zheng, Amir Hossein Tavabi, Jan Caron, Chiming Jin, Haifeng Du, András Kovács, Mingliang Tian, Michael Farle, and Rafal E. Dunin-Borkowski. Magnetic Skyrmion Formation at Lattice Defects and Grain Boundaries Studied by Quantitative Off-Axis Electron Holography. *Nano Letters*, 17(3):1395–1401, 2017.

[45] S M\"uhlbauer, B. Binz, F. Jonietz, C Pfleiderer, A Rosch, A Neubauer, Robert Georgii, and P B\"oni. Skyrmion Lattice in a Chiral Magnet. *Science*, (September):915–920, 2009.

[46] S. A. Meynell, A. Spitzig, B. Edwards, M. D. Robertson, D. Kalliecharan, L. Kreplak, and T. L. Monchesky. Structure of MnSi on SiC(0001). *Physical Review B*, 94(18):184416, 2016.

[47] S. A. Meynell, M. N. Wilson, H. Fritzsche, A. N. Bogdanov, and T. L. Monchesky. Surface twist instabilities and skyrmion states in chiral ferromagnets. *Physical Review B - Condensed Matter and Materials Physics*, 90(1):1–8, 2014.

[48] S. A. Meynell, M. N. Wilson, K. L. Krycka, B. J. Kirby, H. Fritzsche, and T. L. Monchesky. Neutron study of in-plane skyrmions in MnSi thin films. 054402(111):1–10, 2017.

[49] S. A. Meynell, M. N. Wilson, J. C. Loudon, A. Spitzig, F. N. Rybakov, M. B. Johnson, and T. L. Monchesky. Hall effect and transmission electron microscopy of epitaxial MnSi thin films. *Physical Review B - Condensed Matter and Materials Physics*, 90(22):1–10, 2014.

[50] Simon Meynell. Exploring the atomic structure of MnSi (111)/ SiC (0001) with RHEED. (111):1–33, 2015.

[51] Theodore Lloyd Monchesky. *Magnetoresistance and Magnetic Properties of Magnetic Multilayers Grown Directly on GaAs (001)*. PhD thesis, University of Toronto, 2000.

[52] Tôru Moriya. Spin Fluctuations in Itinerant Electron Magnetism, 1985.

[53] A. Neubauer, C. Pfleiderer, B. Binz, A. Rosch, R. Ritz, P. G. Niklowitz, and P. Böni. Topological hall effect in the a phase of MnSi. *Physical Review Letters*, 102(18):1–4, 2009.

[54] C. Pappas, E. Leli??vre-Berna, P. Falus, P. M. Bentley, E. Moskvin, S. Grigoriev, P. Fouquet, and B. Farago. Chiral paramagnetic skyrmion-like phase in MnSi. *Physical Review Letters*, 102(19):1–4, 2009.

[55] C Pfleiderer, A Neubauer, S Mühlbauer, F Jonietz, M Janoschek, S Legl, R Ritz, W Münzer, C Franz, P G Niklowitz, T Keller, R Georgii, P Böni, B Binz, and A Rosch. Quantum order in the chiral magnet MnSi. *Journal of Physics: Condensed Matter*, 21:279801–279801, 2009.

[56] Udo W. Pohl. *Epitaxy of Semiconductors: Introduction to Physical Principles*. 2013.

[57] D. C. Ralph and M. D. Stiles. Spin transfer torques. *Journal of Magnetism and Magnetic Materials*, 320(7):1190–1216, 2008.

[58] U K Rößler, a N Bogdanov, and C Pfleiderer. Spontaneous skyrmion ground states in magnetic metals. *Nature*, 442(7104):797–801, 2006.

[59] T.H.R. Skyrme. A unified field theory of mesons and baryons. *Nuclear Physics*, 31:556–569, 1962.

[60] J.C. Slonczewski. Current-driven excitation of magnetic multilayers. *Journal of Magnetism and Magnetic Materials*, 159(1-2):L1–L7, 1996.

[61] J Smit. The Spontaneous Hall Effect in Ferromagnetics II. *Physica*, XXIV:39–51, 1958.

[62] S. L. Sondhi, A. Karlhede, S. A. Kivelson, and E. H. Rezayi. Skyrmions and the crossover from the integer to fractional quantum Hall effect at small Zeeman energies. *Physical Review B*, 47(24):16419–16426, 1993.

[63] Alyson Spitzig. MnSi thin film growth on SiC substrates in search of out-of-plane skyrmions List of Figures. 2015.

[64] S M Stishov, A E Petrova, S Khasanov, G Kh Panova, A A Shikov, J C Lashley, D Wu, and T A Lograsso. Heat capacity and thermal expansion of the itinerant helimagnet MnSi. *Journal of Physics: Condensed Matter*, 20(23):235222, 2008.

[65] Carl V. Thompson. Solid-State Dewetting of Thin Films. *Annual Review of Materials Research*, 42(1):399–434, 2012.

[66] Y Tokunaga, X Z Yu, J S White, H M Rønnow, D Morikawa, Y Taguchi, and Y Tokura. A new class of chiral materials hosting magnetic skyrmions beyond room temperature. *Nature Communications*, 6(May):7638, 2015.

[67] M. Tsoi, R. E. Fontana, and S. S P Parkin. Magnetic domain wall motion triggered by an electric current. *Applied Physics Letters*, 83(13):2617–2619, 2003.

[68] E. Y. Tsymbal and D. G. Pettifor. Perspectives of giant magnetoresistance. *Solid State Physics - Advances in Research and Applications*, 56(C):113–237, 2001.

[69] Ulrich K. Rößler, Andrei A Leonov, and Alexei N Bogdanov. Chiral Skyrmionic matter in non-centrosymmetric magnets. *Journal of Physics: Conference Series*, 303(1):13, 2011.

[70] Arne Vansteenkiste, Jonathan Leliaert, Mykola Dvornik, Mathias Helsen, Felipe Garcia-Sanchez, and Bartel Van Waeyenberge. The design and verification of MuMax3. *AIP Advances*, 4(10), 2014.

[71] J. A. Venables. *Introduction to surface and thin film processes.* Cambridge, 2003.

[72] M. N. Wilson, A. B. Butenko, A. N. Bogdanov, and T. L. Monchesky. Chiral skyrmions in cubic helimagnet films: The role of uniaxial anisotropy. *Physical Review B - Condensed Matter and Materials Physics*, 89(9):1–13, 2014.

[73] M. N. Wilson, E. A. Karhu, D. P. Lake, A. S. Quigley, S. Meynell, A. N. Bogdanov, H. Fritzsche, U. K. Rößler, and T. L. Monchesky. Discrete helicoidal states in chiral magnetic thin films. *Physical Review B - Condensed Matter and Materials Physics*, 88(21):1–6, 2013.

[74] M. N. Wilson, E. A. Karhu, A. S. Quigley, U. K. Rößler, A. B. Butenko, A. N. Bogdanov, M. D. Robertson, and T. L. Monchesky. Extended elliptic skyrmion gratings in epitaxial MnSi thin films. *Physical Review B - Condensed Matter and Materials Physics*, 86(14):1–6, 2012.

[75] Murray Neff Wilson. *Magnetic Skyrmion Phase in MnSi Thin Films.* PhD thesis, Dalhousie University, 2013.

[76] Tomoyuki Yokouchi, Naoya Kanazawa, Atsushi Tsukazaki, Yusuke Kozuka, Akiko Kikkawa, Yasujiro Taguchi, Masashi Kawasaki, Masakazu Ichikawa, Fumitaka Kagawa, and Yoshinori Tokura. Formation of in-plane skyrmions in epitaxial MnSi thin films as revealed by planar Hall effect. *Journal of the Physical Society of Japan*, 84(10):1–5, 2015.

[77] X. Z. Yu, Y. Onose, N. Kanazawa, J. H. Park, J. H. Han, Y. Matsui, N. Nagaosa, and Y. Tokura. Real-space observation of a two-dimensional skyrmion crystal. *Nature*, 465(7300):901–904, 2010.

[78] Shinji Yuasa, Taro Nagahama, Akio Fukushima, Yoshishige Suzuki, and Koji Ando. Giant room-temperature magnetoresistance in single-crystal Fe/MgO/Fe magnetic tunnel junctions. *Nature Materials*, 3(12):868–871, 2004.

[79] Xichao Zhang, Motohiko Ezawa, and Yan Zhou. Magnetic skyrmion logic gates: conversion, duplication and merging of skyrmions. *Scientific Reports*, 5:9400, 2015.

Copyright permissions

AMERICAN PHYSICAL SOCIETY ORDER DETAILS

Aug 21, 2017

Order Number	501300084
Order date	Aug 21, 2017
Licensed Content Publisher	American Physical Society
Licensed Content Publication	Physical Review B
Licensed Content Title	Structure of MnSi on SiC(0001)
Licensed Content Author	S. A. Meynell et al.
Licensed Content Date	Nov 14, 2016
Licensed Content Volume	94
Type of Use	Thesis/Dissertation
Requestor type	Student
Format	Print, Electronic
Portion	chart/graph/table/figure
Number of charts/graphs/tables/figures	6
Portion description	Fig. 3 d), Fig. 4, Fig. 5 c) and d), Fig. 6, Fig. 8, Fig. 9
Rights for	Main product
Duration of use	Life of Current Edition
Creation of copies for the disabled	no
With minor editing privileges	yes
For distribution to	Worldwide
In the following language(s)	Original language of publication
With incidental promotional use	no
The lifetime unit quantity of new product	0 to 499
The requesting person/organization is:	Simon Meynell, Dalhousie
Order reference number	
Title of your thesis / dissertation	The Effect of Strain in MnSi Thin Films and the Stability of In-Plane Skyrmions
Expected completion date	Aug 2017
Expected size (number of pages)	92
Requestor Location	Mr. Simon Meynell 2003 Maynard St. Halifax, NS B3K3T1 Canada Attn: Mr. Simon Meynell
Total	Not Available

AMERICAN PHYSICAL SOCIETY ORDER DETAILS

Aug 21, 2017

Order Number	501300085
Order date	Aug 21, 2017
Licensed Content Publisher	American Physical Society
Licensed Content Publication	Physical Review B
Licensed Content Title	Neutron study of in-plane skyrmions in MnSi thin films
Licensed Content Author	S. A. Meynell et al.
Licensed Content Date	Aug 1, 2017
Licensed Content Volume	96
Type of Use	Thesis/Dissertation
Requestor type	Student
Format	Print, Electronic
Portion	chart/graph/table/figure
Number of charts/graphs/tables/figures	4
Portion description	Fig. 1, Fig. 2, Fig. 4, Fig. 5
Rights for	Main product
Duration of use	Life of Current Edition
Creation of copies for the disabled	no
With minor editing privileges	yes
For distribution to	Worldwide
In the following language(s)	Original language of publication
With incidental promotional use	no
The lifetime unit quantity of new product	0 to 499
The requesting person/organization is:	Simon Meynell, Dalhousie
Order reference number	
Title of your thesis / dissertation	The Effect of Strain in MnSi Thin Films and the Stability of In-Plane Skyrmions
Expected completion date	Aug 2017
Expected size (number of pages)	92
Requestor Location	Mr. Simon Meynell 2003 Maynard St.
	Halifax, NS B3K3T1 Canada Attn: Mr. Simon Meynell
Total	Not Available

AMERICAN PHYSICAL SOCIETY ORDER DETAILS

Aug 21, 2017

Order Number	501300088
Order date	Aug 21, 2017
Licensed Content Publisher	American Physical Society
Licensed Content Publication	Physical Review B
Licensed Content Title	Chiral skyrmions in cubic helimagnet films: The role of uniaxial anisotropy
Licensed Content Author	M. N. Wilson et al.
Licensed Content Date	Mar 12, 2014
Licensed Content Volume	89
Type of Use	Thesis/Dissertation
Requestor type	Student
Format	Print, Electronic
Portion	chart/graph/table/figure
Number of charts/graphs/tables/figures	1
Portion description	Fig. 3
Rights for	Main product
Duration of use	Life of Current Edition
Creation of copies for the disabled	no
With minor editing privileges	yes
For distribution to	Worldwide
In the following language(s)	Original language of publication
With incidental promotional use	no
The lifetime unit quantity of new product	0 to 499
The requesting person/organization is:	Simon Meynell, Dalhousie
Order reference number	
Title of your thesis / dissertation	The Effect of Strain in MnSi Thin Films and the Stability of In-Plane Skyrmions
Expected completion date	Aug 2017
Expected size (number of pages)	92
Requestor Location	Mr. Simon Meynell 2003 Maynard St.
	Halifax, NS B3K3T1 Canada Attn: Mr. Simon Meynell
Total	Not Available

Order Number	501300087
Order date	Aug 21, 2017
Licensed Content Publisher	American Physical Society
Licensed Content Publication	Physical Review B
Licensed Content Title	Discrete helicoidal states in chiral magnetic thin films
Licensed Content Author	M. N. Wilson et al.
Licensed Content Date	Dec 20, 2013
Licensed Content Volume	88
Type of Use	Thesis/Dissertation
Requestor type	Student
Format	Print, Electronic
Portion	chart/graph/table/figure
Number of charts/graphs/tables/figures	1
Portion description	Fig. 1 a)
Rights for	Main product
Duration of use	Life of Current Edition
Creation of copies for the disabled	no
With minor editing privileges	yes
For distribution to	Worldwide
In the following language(s)	Original language of publication
With incidental promotional use	no
The lifetime unit quantity of new product	0 to 499
The requesting person/organization is:	Simon Meynell, Dalhousie
Order reference number	
Title of your thesis / dissertation	The Effect of Strain in MnSi Thin Films and the Stability of In-Plane Skyrmions
Expected completion date	Aug 2017
Expected size (number of pages)	92
Requestor Location	Mr. Simon Meynell 2003 Maynard St. Halifax, NS B3K3T1 Canada Attn: Mr. Simon Meynell
Total	Not Available